Journal of the Mechanics and Physics of Solids 140 (2020) 103941

Contents lists available at ScienceDirect

Journal of the Mechanics and Physics of Solids

journal homepage: www.elsevier.com/locate/jmps

Rupture of 3D-printed hyperelastic composites: Experiments and phase field fracture modeling

Jonathan Russ[a,*], Viacheslav Slesarenko[b,c], Stephan Rudykh[d], Haim Waisman[a]

[a] Columbia University, Department of Civil Engineering and Engineering Mechanics, New York, NY 10027, United States
[b] Aerospace Engineering, Technion, Israel Institute of Technology, Haifa, 32003, Israel
[c] Lavrentyev Institute of Hydrodynamics of SB RAS, Lavrentyev av., 15, Novosibirsk, 630090, Russia
[d] Department of Mechanical Engineering, University of Wisconsin-Madison, Madison, WI 53706, United States

ARTICLE INFO

Article history:
Received 24 January 2020
Revised 26 February 2020
Accepted 17 March 2020
Available online 1 April 2020

Keywords:
3D-Printing
Phase field fracture
Rupture
Hyperelasticity
Digital image correlation

ABSTRACT

In this work, we study the failure behavior of 3D-printed polymer composites undergoing large deformations. Experimental results are compared to numerical simulations using the phase field fracture method with an energetic threshold and an efficient plane-stress formulation. The developed framework is applied to a composite system consisting of three stiff circular inclusions embedded into a soft matrix. In particular, we examine how geometrical parameters, such as the distances between inclusions and the length of initial notches, affect the failure pattern in the soft composites. We observe complex failure sequences including crack arrest and secondary crack initiation in the bulk material. Remarkably, our numerical simulations capture these essential features of the composite failure behavior and the numerical results are in good agreement with the experiments. We find that the performance of composites – their strength and toughness – can be tuned through selection of the inclusion position. We report, however, that the optimal inclusion spacing is not unique and depends also on the initial notch length. These findings offer useful insight for design of soft composite materials with enhanced performance.

© 2020 Elsevier Ltd. All rights reserved.

1. Introduction

Polymer composites are versatile high performance materials that are widely used in a variety of engineering applications. These materials, consisting of a polymer matrix reinforced by hard-inclusions, offer significant advantages over pure polymers. For example, well-designed combinations of these components may lead to superior mechanical and thermal properties that are infeasible using a single material (Greenhalgh, 2009). In particular, since the strength and stiffness of the inclusions are typically much higher than those of the matrix material, the stiffness of the composite is typically improved in addition to the material toughness due to the treacherous path cracks must traverse through the matrix in order for a structure to fail catastrophically.

The use of 3D-printing for rapid manufacturing of polymer composites has gained significant attention in the last two decades (Wang et al., 2017). This additive manufacturing technique can produce polymer composites with complex geometries and precise inclusion positions/shapes obtained directly from computer aided designs. However, while the addition of inclusions in a polymer matrix may enhance its strength (resistance to non-recoverable deformation), it may also decrease

* Corresponding author.
E-mail address: jr3737@columbia.edu (J. Russ).

https://doi.org/10.1016/j.jmps.2020.103941
0022-5096/© 2020 Elsevier Ltd. All rights reserved.

its toughness (resistance to fracture) (Ritchie, 2011). In particular, a different arrangement of inclusions may entirely alter the failure pattern of the polymer composite, thereby affecting its fracture toughness.

Theoretical and numerical predictions together with the observed performance of natural and biological materials indicate that microstructural design holds significant potential for the development of superior materials. The physical realization of these ideas relies on advances in material fabrication techniques and the ability to produce microstructures at various length scales. Thus, for example, Slesarenko et al. (2017a,b) experimentally realized the underlining failure mechanisms in nacre-like 3D-printed composite structures. In particular, they observed distinct single-step and two-step failure modes in the soft interphases depending on the loading direction relative to microstructures. Buehler and co-authors (Dimas et al., 2013; Libonati et al., 2016) employed 3D-printing to illustrate the improved toughness performance of the numerically predicted bio-inspired composites based on mineralized natural materials with soft interphases. Ryvkin et al. (2020) realized fault-tolerant lattice structures through pre-designed failure in weak links, thus, preventing damage propagation, and promoting even damage distribution. Alternative strategies such as crack tip blunting (Dimas et al., 2013), microstructure-guided crack deflection (Studart, 2016), and shielding (Jia et al., 2019) have been successfully illustrated on 3D-printed composites. Liu and Li (2018) reported increased fracture toughness in 3D-printed composites due to weak wavy interfaces. We note, however, that the fracture behavior of the soft materials is rate-sensitive (Slesarenko and Rudykh, 2018), and this aspect can play an important role in the failure mechanisms of dynamically loaded composites (Gu et al., 2017).

Computational modeling of the rupture of polymer composites at large deformations remains a significant challenge. Beyond the hyperelastic material modeling and complex geometries, numerical methods that attempt to model fracture must be able to capture crack nucleation at multiple arbitrary spatial locations and crack propagation along complex trajectories while accounting for crack coalescence and branching. Furthermore, these methods should also be numerically robust (e.g. capable of handling large element distortions), insensitive to the choice of mesh discretization, and well-posed (e.g. convergent under mesh refinement).

The phase field method is one such promising method that has emerged in the past two decades (Bourdin et al., 2008; Francfort and Marigo, 1998; Miehe et al., 2010a; 2015; 2010b), and has already been explored in a variety of areas including quasi-brittle fracture (Ambati et al., 2015; Borden et al., 2012; Duda et al., 2015; Nguyen et al., 2016), ductile fracture (Ambati et al., 2016; Arriaga and Waisman, 2017; Borden et al., 2016; McAuliffe and Waisman, 2015), fracture of geological materials including hydraulic fracture (Choo and Sun, 2018; Miehe and Mauthe, 2016; Mikelić et al., 2015; Wilson and Landis, 2016), interfacial fracture (Nguyen et al., 2016; Paggi and Reinoso, 2017; Verhoosel and Borst, 2013), anisotropic fracture (Teichtmeister et al., 2017), bone fracture (Shen et al., 2019), and fracture of viscoelastic materials (Shen et al., 2019). In the phase field method, the discrete crack surface is approximated by a diffusive crack representation via an auxiliary scalar field. The evolution of the fracture surface is captured by an additional PDE, which can be derived variationally (Bourdin et al., 2008) or using thermodynamic principles (McAuliffe and Waisman, 2015). Most phase field methods published in the literature require only two parameters: one controlling the width of the diffusive fracture surface l_0, and either the critical energy release rate, G_c, or the critical tensile energy density Ψ_c, which may be viewed as material parameters.

In the context of large strain fracture of hyperelastic materials, several notable phase field fracture methods have been published. Miehe and Schnzel (2014) was the first to propose large deformation brittle fracture formulation for rubbery polymers. Wu et al. (2016) proposed a stochastic fracture analysis of the rupture of rubber reinforced with Carbon black random inclusions, which provided insight into better designs of these composites. Subsequent work by San and Waisman proposed to optimize the location of these particles in a soft polymer matrix to achieve failure resistant designs (San and Waisman, 2017).

Raina and Miehe (2016) and Gltekin et al. (2018) studied the fracture of soft biological tissues accounting for anisotropic hyperelasticity with different fiber orientations. Talamini et al. Talamini et al. (2018) proposed a new energy split in the phase field formulation to account for chain bond deformation, which resulted in a modified phase field driving force. This formulation was later extended by Mao and Anand (2018) to model fracture of polymeric gel. Bilgen and Weinberg (2019) also developed new ad-hoc driving forces, which were motivated by general fracture mechanical considerations. Kumar et al. (2018) derived toughness functions to model the fracture and healing of elastomers undergoing large deformations. Yin et al. (2019) studied fracture of exotic natural structures (Bouligand structures), and compared their numerical results with 3D-printed samples. Additionally, rate dependent visco-hyperelastic rubber fracture has been studied by Loew et al. (2019) and Yin and Kaliske (2019).

It should be noted that, as with most numerical methods, there are also drawbacks of the phase field method when compared with other techniques. A few important cons, such as the computational cost, are discussed in the work of Wu et al. (2019). Advancements in mesh adaptivity seek to alleviate some of the computational burden (see Heister et al. (2015) for example). Additionally, in classical phase field models the strength of the material is tied to the length scale (see Borden et al. (2012) for 1D analysis). In the current work we select a length scale on the same order as one previously identified for a rubber material (Loew et al., 2019) and use the phase field formulation with an energetic threshold presented in Miehe et al. (2015). This allows us to select the critical strain energy density such that phase field evolution occurs only after the local strain energy density exceeds this threshold. The idea of using the strain energy density as a failure criterion is also consistent with the findings of Hocine et al. (2002) in which failure of natural rubber was investigated and the strain energy density along the crack trajectory was found to be independent of the crack length and specimen geometry (see also Volokh, 2010).

Additionally, it is important to note that other interesting failure models for soft materials have been proposed. In particular, the work of Volokh on hyperelasticity with softening, based on the idea of energy limiters, and more recently the material sink formulation (Faye et al., 2019; Volokh, 2011; 2017) also seems to be promising.

In this work we study the failure mechanism of 3D-printed polymer composites undergoing large deformation through experiments and numerical modeling. A simple parameterized geometry with three rigid circular inclusions embedded into a soft hyperelastic matrix is proposed for a test study. By adjusting the distances between inclusions and by introducing notches of various lengths we alter the failure pattern in the specimens. A non-standard phase field fracture method with energetic threshold is employed for the numerical study assuming plane stress conditions. Remarkably, the derived and implemented reduced plane stress formulation coupled with phase field fracture agrees well with the experimental data, capturing both crack arrest and secondary crack initiation in the bulk material.

We remark that the material fabrication technique employed in this study does not result in weak interfaces between the matrix and inclusion phases, and, for various composite systems (Li and Rudykh, 2019; Li et al., 2018a; 2018b; 2013; Rudykh and Boyce, 2014; Rudykh et al., 2015; Slesarenko and Rudykh, 2016), failure in this region has not been observed. We note, however, that the composite fabrication method produces the interphase mixing zone (see, for example, Arora et al. (2019) that studied the influence of the inhomogeneous interphases on mechanical stability). Our experimental observations indicate that the matrix is weaker than the interphase material. Nevertheless, the numerical formulation could potentially be extended to the class of composites with weak interphases by adopting, for example, a framework appropriately capturing the relevant physics (see, for example, Nguyen et al. (2016)).

The paper is organized as follows: In Section 2 we provide the details of the phase field fracture model employed herein and the corresponding finite element implementation. In Section 3 the composite structures are detailed and the experimental/numerical methods used to study their failure behavior are outlined. Finally the numerical and experimental results are provided in Section 4 in which both qualitative and quantitative features are compared. Furthermore, the numerical model is also used in place of additional experimental data to remark on the physical implications of the results obtained, followed by a concluding summary.

2. Phase field fracture model

In this section we provide the derivation of the phase field fracture formulation used in this work, which is largely based on the seminal work of Francfort and Marigo (1998), Bourdin et al. (2008) and Miehe et al. (2010a, 2015, 2010b). However, we employ a non-standard phase field method with an energetic threshold as presented in Miehe et al. (2015) in order to prevent energy degradation at low stress levels. We note that the same phenomenon could also be partially mitigated by judicious selection of the degradation function as presented by Borden (2012). Experimentally applied loading rates are low enough to permit the use of quasi-static numerical analyses and for reasons of computational efficiency we perform the numerical simulations in two space dimensions under an assumed state of plane stress. In Appendix A the plane stress assumption is justified for the geometry used herein via numerical comparison with a plane strain assumption and a full three-dimensional formulation. Additionally, since the plane stress assumption results in a constraint that is not trivially satisfied, we also derive the reduced in-plane relations, including the nonlinear equation to be solved for the out-of-plane stretch and the analytical reduced consistent tangent tensor.

2.1. Phase field fracture formulation

Consistent with the ideas presented in Francfort and Marigo (1998), the phase field fracture formulation used herein is posed as an energy minimization problem for a continuum body, Ω_0 (where the $(\cdot)_0$ subscript signifies the reference configuration). Here we let $\boldsymbol{F}$ represent the deformation gradient and Γ_0 represent the crack surface. Neglecting the potential associated with external forces, the total potential energy of the solid may be expressed as

$$\Pi(\boldsymbol{F}, \Gamma_0) = W_{elas}(\boldsymbol{F}) + W_{frac}(\Gamma_0) \tag{2.1}$$

in which the stored elastic energy, W_{elas}, is a function of the deformation gradient ($\boldsymbol{F}$), and the fracture surface energy, W_{frac}, depends on the crack surface. In the phase field formulation the crack surface is approximated by an elliptic functional of a scalar field, $d \in [0, 1]$, which may be expressed as

$$\Gamma_0 \approx \Gamma_{l_0}(d) = \int_{\Omega_0} \gamma(d, \nabla_0\, d) dV = \int_{\Omega_0} \left(\frac{1}{2l_0} d^2 + \frac{l_0}{2} \nabla_0\, d \cdot \nabla_0\, d \right) dV \tag{2.2}$$

where $\gamma(d, \nabla_0\, d)$ is termed the crack surface density function. The minimization of this functional yields the diffuse crack topology (Bourdin et al., 2008; Miehe et al., 2010b) which replaces the sharp crack representation.

$$d(\boldsymbol{X}) = \mathrm{Arg}\left\{ \inf_{d \in \mathcal{S}_\Gamma} \Gamma_{l_0}(d) \right\} \tag{2.3}$$

$$\mathcal{S}_\Gamma = \{ d \mid d \in H^1,\ d(\boldsymbol{X}) = 1 \text{ when } \boldsymbol{X} \in \Gamma \} \tag{2.4}$$

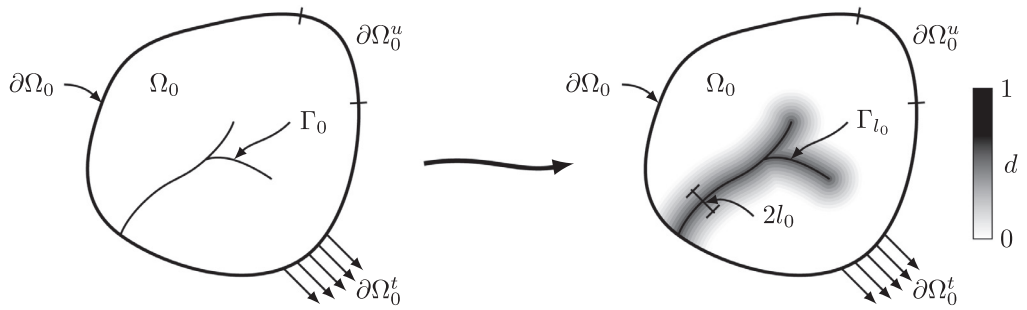


Fig. 1. Phase field approximation of a sharp crack discontinuity in a hyperelastic medium. Note that both figures are drawn in the reference configuration.

The length scale, l_0, that is introduced controls the width of the regularized fracture surface (see Fig. 1). We define $\mathcal{S}_\Gamma$ as the set of admissible fields satisfying the Dirichlet-type conditions on the crack surface, where $\boldsymbol{X}$ signifies the spatial location in the undeformed domain, and H^1 is the Sobolev function space given as

$$H^1 = \left\{ v \;\middle|\; \int_{\Omega_0} v^2 d\boldsymbol{X} < +\infty, \text{ and } \int_{\Omega_0} |\nabla v|^2 d\boldsymbol{X} < +\infty \right\} \tag{2.5}$$

As presented in Miehe et al. (2010b), an approximation of the fracture surface energy is obtained using the crack surface approximation provided in Eq. 2.2. Subsequently, in Miehe et al. (2015), a strain criterion with a threshold was introduced in order to prevent degradation of the elastic energy at low stress levels. This updated model is used in this work where the fracture surface energy approximation may be expressed as

$$\hat{W}_{frac}(d) = \int_{\Omega_0} 2\Psi_c \left(d + \frac{l_0^2}{2} \nabla_0 \, d \cdot \nabla_0 \, d \right) dV \tag{2.6}$$

in which Ψ_c represents a critical fracture energy per unit volume. In this work we use Ψ_c as a material parameter for calibration of the model with the experimental data.

2.1.1. Stored elastic energy approximation

The undamaged elastic energy density employed in this work consists of a standard decomposition into volumetric and isochoric components as shown below. The isochoric function is a simple neoHookean model with shear modulus, μ, while the volumetric function is another common form with bulk modulus, κ. Here we define the elastic energy density function per unit undeformed volume,

$$\Psi_e(\boldsymbol{F}) = \Psi_e(\bar{I}_1, J) = \underbrace{\frac{\kappa}{2}(\log J)^2}_{\Psi_e^{vol}} + \underbrace{\frac{\mu}{2}\left(\bar{I}_1 - 3\right)}_{\Psi_e^{iso}} \tag{2.7}$$

where $J = \det \boldsymbol{F}$ and $\bar{I}_1 = J^{-2/3} I_1$ which is the first invariant of the isochoric right Cauchy-Green deformation tensor and $I_1 = F_{ij}F_{ij}$ is the unmodified first invariant. This elastic energy density adequately describes the elastic response of the material and may be naturally decomposed into compressive and tensile components via a volumetric/isochoric energy split similar to that of Amor et al. Amor et al. (2009). Here we define this tensile/compressive (Ψ_e^+/Ψ_e^-) energy decomposition in the following way based upon the determinant of the deformation gradient similar to Wu et al. (2016).

$$\Psi_e^+(\bar{I}_1, J) = \begin{cases} \frac{\kappa}{2}(\log J)^2 + \frac{\mu}{2}\left(\bar{I}_1 - 3\right), & \text{if } J \geq 1 \\ \frac{\mu}{2}\left(\bar{I}_1 - 3\right), & \text{otherwise} \end{cases} \tag{2.8}$$

$$\Psi_e^-(\bar{I}_1, J) = \Psi_e(\bar{I}_1, J) - \Psi_e^+(\bar{I}_1, J) \tag{2.9}$$

Note that other splits of the elastic energy are possible, including one based on a multiplicative split of the deformation gradient (Hesch and Weinberg, 2014), one based on principal invariants of the Cauchy-Green deformation tensor (Hesch et al., 2017), and a more recent split based on principal stretches (Tang et al., 2019).

This yields a damaged elastic energy density in which only the tensile energy is degraded according to Miehe et al. (2010a),

$$\Psi_e(\bar{I}_1, J, d) = \Psi_e^-(\bar{I}_1, J) + (g(d) + k)\Psi_e^+(\bar{I}_1, J) \tag{2.10}$$

where the total stored elastic energy approximation is obtained via integration over the reference volume.

$$\hat{W}_{elas}(\bar{I}_1, J, d) = \int_{\Omega_0} \Psi_e(\bar{I}_1, J, d) dV \tag{2.11}$$

The phase field parameter, d, affects the stored elastic energy via the action of the so-called degradation function, $g(d)$. Although a cubic degradation function has previously been proposed (Borden, 2012), we employ the more common quadratic degradation function in this work, defined as $g(d) = (1-d)^2$. Additionally, we include the small constant parameter, k, in order to ensure the problem remains well-posed (Miehe et al., 2010b). In all subsequent examples in this work k is set to 10^{-6}.

The damaged first Piola-Kirchoff stress may then be obtained directly from the damaged elastic energy density via the following relation,

$$\boldsymbol{P} = \underbrace{\frac{\partial \Psi_e^-}{\partial \boldsymbol{F}}}_{\boldsymbol{P}^-} + (g(d)+k)\underbrace{\frac{\partial \Psi_e^+}{\partial \boldsymbol{F}}}_{\boldsymbol{P}^+} \tag{2.12}$$

where $\boldsymbol{P}$ is now the damaged first Piola-Kirchoff stress tensor and $\boldsymbol{P}^-/\boldsymbol{P}^+$ are the undamaged, compressive and tensile first Piola-Kirchoff stress tensors, respectively.

2.1.2. Approximate total potential energy

Substituting the above approximations into the total potential energy in Eq. (2.1) we obtain the approximate form ($\tilde{\Pi}$) as

$$\begin{aligned}\tilde{\Pi}(\boldsymbol{u}, d) &= \hat{W}_{elas}(\boldsymbol{F}, d) + \hat{W}_{frac}(d) \\ &= \int_{\Omega_0} \left(\Psi_e^-(\boldsymbol{F}) + (g(d)+k)\Psi_e^+(\boldsymbol{F})\right) dV \\ &\quad + \int_{\Omega_0} 2\Psi_c \left(d + \frac{l_0^2}{2}\nabla_0\, d \cdot \nabla_0\, d\right) dV\end{aligned} \tag{2.13}$$

Note that the hat notation, $\hat{(\cdot)}$, in Eq. (2.13) signifies the previously introduced approximation of the quantity. At a minimum, the first variation of the total potential with respect to the displacement and phase field must vanish, i.e. $\delta\tilde{\Pi} = 0$. Application of this principle, the divergence theorem, and the standard variational argument yields the Euler-Lagrange equations,

$$\nabla_0 \cdot \boldsymbol{P} = \boldsymbol{0} \quad \text{in } \Omega_0 \tag{2.14}$$

$$\Psi_c\left(d - l_0^2 \nabla_0 \cdot \nabla_0\, d\right) - (1-d)(\Psi_e^+ - \Psi_c) = 0 \quad \text{in } \Omega_0 \tag{2.15}$$

$$\boldsymbol{u} = \hat{\boldsymbol{u}} \quad \text{on } \partial\Omega_0^u \tag{2.16}$$

$$\boldsymbol{n} \cdot \nabla_0\, d = 0 \quad \text{on } \partial\Omega_0 \tag{2.17}$$

where the additional Dirichlet and Neumann boundary conditions have been added (i.e. Eqs. (2.16) and (2.17)). Note that the Eq. (2.17) implies that there is no damage flux out of the domain. Eq. (2.14) represents quasi-static equilibrium in the absence of body forces while Eq. (2.15) governs the evolution of the phase field.

Finally, Eq. (2.15) is modified in order to enforce irreversibility of crack growth. The local history field, $\mathcal{H}$, proposed in Miehe et al. (2010a), is used in order to ensure the local crack driving force is nondecreasing. Note that in the equation below, t, is a pseudo-time variable related to the incremental external loading. Additionally, we employ the purely numerical viscous regularization with viscosity parameter, η, phase field at the previous time increment, d_n, and time increment, Δt, presented by Miehe et al. (2010a, 2015). The reader is referred to these works for additional details regarding this numerical regularization. This viscous term is included in the quasi-static setting in order to prevent large jumps in the crack length over a given time increment. In the context large deformations, this is particularly important since large jumps in crack length are also typically accompanied by large changes in the displacement field which may result in inverted elements during the displacement update and potential failure of the simulation. The final equation governing the evolution of the phase field is provided below.

$$\eta\frac{d - d_n}{\Delta t} + \Psi_c\left(d - l_0^2\nabla_0 \cdot \nabla_0\, d\right) - (1-d)\mathcal{H} = 0 \tag{2.18}$$

$$\text{where } \mathcal{H}(\boldsymbol{X}, t) = \max_{\tau\in[0,t]} \left\langle \Psi_e^+(\boldsymbol{X}, \tau) - \Psi_c \right\rangle_+ \tag{2.19}$$

Note that the Macaulay brackets are defined such that $\langle\cdot\rangle_+ = \max(\cdot, 0)$.

2.1.3. Plane stress enforcement

The experiments presented herein are generally well-represented by a state of plane stress. Due to the large computational burden of the three-dimensional formulation, we reduce the equations to a two-dimensional plane stress state. The derivation of the reduced first Piola-Kirchoff stress and the associated analytical consistent tangent are provided in this section.

We begin with the specific three-dimensional first Piola-Kirchoff stress as obtained from the undamaged stored elastic energy density provided in Eq. (2.7).

$$\boldsymbol{P} = \frac{\partial \Psi_e(\bar{I}_1, J)}{\partial \boldsymbol{F}} = \kappa \log(J)\boldsymbol{F}^{-T} + \mu J^{-2/3}\left(\boldsymbol{F} - \frac{I_1}{3}\boldsymbol{F}^{-T}\right) \tag{2.20}$$

The Kirchoff stress may then be obtained via right multiplication of the deformation gradient transpose, resulting in

$$\boldsymbol{\tau} = \boldsymbol{P}\cdot\boldsymbol{F}^T = \kappa \log(J)\boldsymbol{I} + \mu J^{-2/3}\left(\boldsymbol{B} - \frac{I_1}{3}\boldsymbol{I}\right) \tag{2.21}$$

in which $\boldsymbol{I}$ represents the second order identity tensor and $\boldsymbol{B} = \boldsymbol{F}\boldsymbol{F}^T$ signifies the left Cauchy-Green deformation tensor. For a state of plane stress we have the following constraints on the Kirchoff stress (equivalently, these represent constraints on the Cauchy stress since the two stress measures only differ by the positive scalar multiple, J),

$$\tau_{13} = \tau_{31} = 0 \Rightarrow B_{13} = B_{31} = 0 \tag{2.22}$$

$$\tau_{23} = \tau_{32} = 0 \Rightarrow B_{23} = B_{32} = 0 \tag{2.23}$$

$$\tau_{33} = \kappa \log(J) + \mu J^{-2/3}\left(B_{33} - \frac{I_1}{3}\right) = 0 \tag{2.24}$$

Assuming that the deformation gradient takes the following structure,

$$\boldsymbol{F} = \begin{bmatrix} F_{11} & F_{12} & 0 \\ F_{21} & F_{22} & 0 \\ 0 & 0 & \lambda \end{bmatrix} \tag{2.25}$$

where λ is the out-of-plane stretch, one sees that Eqs. (2.22) and (2.23) are automatically satisfied. Eq. (2.24), however, cannot be trivially satisfied and reduces to the following nonlinear equation.

$$f \equiv \lambda^2 + \frac{\kappa}{\mu}J^{2/3}\log(J) + \frac{I_1}{3} = 0 \tag{2.26}$$

Subsequently, the constitutive equations are reduced by using indicial notation combined with Einstein's summation convention where Greek indices may vary from 1 to 2 only and represent the tensorial in-plane components. Defining the following reduced invariants,

$$i_1 = F_{\alpha\beta}F_{\alpha\beta} \tag{2.27}$$

$$j = F_{11}F_{22} - F_{12}F_{21} \tag{2.28}$$

we have $I_1 = i_1 + \lambda^2$ and $J = j\lambda$, reducing Eq. (2.26) to

$$f \equiv \lambda^2 + \frac{3\kappa}{2\mu}(j\lambda)^{2/3}\log(j\lambda) - \frac{i_1}{2} = 0 \tag{2.29}$$

Due to our choice of elastic energy density, the above scalar equation is nonlinear in the out-of-plane stretch, λ, and is solved numerically with a local newton iteration.

Once λ is determined, the reduced first Piola-Kirchoff stress may be computed via substitution of the above expressions and differentiation of each component with respect to $F_{\alpha\beta}$ to obtain $P_{\alpha\beta} = P^{vol}_{\alpha\beta} + P^{iso}_{\alpha\beta}$.

$$P^{vol}_{\alpha\beta} = \frac{\partial \Psi^{vol}_e}{\partial F_{\alpha\beta}} = \kappa \log(j\lambda)T_{\alpha\beta} \tag{2.30}$$

$$P^{iso}_{\alpha\beta} = \frac{\partial \Psi^{iso}_e}{\partial F_{\alpha\beta}} = \mu(j\lambda)^{-2/3}\left(E_{\alpha\beta} - \frac{i_1 + \lambda^2}{3}T_{\alpha\beta}\right) \tag{2.31}$$

where we have defined,

$$T_{\alpha\beta} \equiv F^{-T}_{\alpha\beta} + \frac{1}{\lambda}\frac{\partial \lambda}{\partial F_{\alpha\beta}} \tag{2.32}$$

$$E_{\alpha\beta} \equiv F_{\alpha\beta} + \lambda \frac{\partial \lambda}{\partial F_{\alpha\beta}} \tag{2.33}$$

The derivative $\frac{\partial \lambda}{\partial F_{\alpha\beta}}$ may be obtained by differentiating Eq. (2.29) with respect to $F_{\alpha\beta}$. After some algebra, the following expression results,

$$\frac{\partial \lambda}{\partial F_{\alpha\beta}} = \frac{F_{\alpha\beta} - \frac{3\kappa}{2\mu}(j\lambda)^{2/3}\left(\frac{2}{3}\log(j\lambda)+1\right)F^{-T}_{\alpha\beta}}{2\lambda + \frac{3\kappa}{2\mu} j^{2/3}\lambda^{-1/3}\left(\frac{2}{3}\log(j\lambda)+1\right)} \tag{2.34}$$

In order to solve the global Newton system efficiently the analytical consistent tangent tensor is derived and used in computation of the global tangent stiffness matrices. Although this derivation is rather long and tedious, we believe that this is an essential component of the method in order to ensure some degree of robustness when coupled with phase field fracture since very large deformations often result.

We begin by defining each component of the consistent tangent separately as is done in Eqs. (2.30) and (2.31) above where the total consistent tangent may be written $\mathbb{C} = \mathbb{C}^{vol} + \mathbb{C}^{iso}$.

$$\mathbb{C}^{vol}_{\alpha\beta\gamma\delta} = \frac{\partial P^{vol}_{\alpha\beta}}{\partial F_{\gamma\delta}} = \kappa \log(j\lambda)\frac{\partial T_{\alpha\beta}}{\partial F_{\gamma\delta}} + \kappa T_{\alpha\beta}T_{\gamma\delta} \tag{2.35}$$

$$\begin{aligned}\mathbb{C}^{iso}_{\alpha\beta\gamma\delta} = \frac{\partial P^{iso}_{\alpha\beta}}{\partial F_{\gamma\delta}} &= \mu\left(E_{\alpha\beta} - \frac{i_1+\lambda^2}{3}T_{\alpha\beta}\right)\frac{\partial (j\lambda)^{-2/3}}{\partial F_{\gamma\delta}} \\ &+ \frac{\mu}{(j\lambda)^{2/3}}\left(\frac{\partial E_{\alpha\beta}}{\partial F_{\gamma\delta}} - \frac{1}{3}\left(\frac{\partial (i_1+\lambda^2)}{\partial F_{\gamma\delta}}T_{\alpha\beta} + (i_1+\lambda^2)\frac{\partial T_{\alpha\beta}}{\partial F_{\gamma\delta}}\right)\right)\end{aligned} \tag{2.36}$$

The unspecified derivatives in the above expressions may then be expressed via the following relations.

$$\frac{\partial (j\lambda)^{-2/3}}{\partial F_{\gamma\delta}} = -\frac{2}{3}(j\lambda)^{-2/3}T_{\gamma\delta} \tag{2.37}$$

$$\frac{\partial (i_1+\lambda^2)}{\partial F_{\gamma\delta}} = 2F_{\gamma\delta} + 2\lambda\frac{\partial \lambda}{\partial F_{\gamma\delta}} \tag{2.38}$$

$$\frac{\partial T_{\alpha\beta}}{\partial F_{\gamma\delta}} = -F^{-1}_{\delta\alpha}F^{-1}_{\beta\gamma} + \frac{1}{\lambda}\frac{\partial^2 \lambda}{\partial F_{\alpha\beta}\partial F_{\gamma\delta}} - \frac{1}{\lambda^2}\frac{\partial \lambda}{\partial F_{\alpha\beta}}\frac{\partial \lambda}{\partial F_{\gamma\delta}} \tag{2.39}$$

$$\frac{\partial E_{\alpha\beta}}{\partial F_{\gamma\delta}} = \delta_{\alpha\gamma}\delta_{\beta\delta} + \lambda\frac{\partial^2 \lambda}{\partial F_{\alpha\beta}\partial F_{\gamma\delta}} + \frac{\partial \lambda}{\partial F_{\alpha\beta}}\frac{\partial \lambda}{\partial F_{\gamma\delta}} \tag{2.40}$$

The final unspecified derivative is the second derivative of the out-of-plane stretch with respect to the in-plane components of the deformation gradient. Labeling the numerator of Eq. (2.34) $N_{\alpha\beta}$ and the denominator D we differentiate each expression and use the quotient rule to obtain the final expression.

$$\text{Let } c_1 \equiv (j\lambda)^{2/3}\left(\log(j\lambda) + \frac{3}{2}\right) \tag{2.41}$$

$$N_{\alpha\beta} \equiv F_{\alpha\beta} - c_1\frac{\kappa}{\mu}F^{-T}_{\alpha\beta} \tag{2.42}$$

$$D \equiv 2\lambda + \frac{\kappa c_1}{\mu\lambda} \tag{2.43}$$

Differentiating the numerator and the denominator of Eq. (2.34) we obtain,

$$\frac{\partial N_{\alpha\beta}}{\partial F_{\gamma\delta}} = -\frac{\kappa}{\mu}\left(F^{-T}_{\alpha\beta}\frac{\partial c_1}{\partial F_{\gamma\delta}} - c_1F^{-1}_{\delta\alpha}F^{-1}_{\beta\gamma}\right) + \delta_{\alpha\gamma}\delta_{\beta\delta} \tag{2.44}$$

$$\frac{\partial D}{\partial F_{\gamma\delta}} = 2\frac{\partial \lambda}{\partial F_{\gamma\delta}} + \frac{\kappa}{\mu}\left(-\frac{c_1}{\lambda^2}\frac{\partial \lambda}{\partial F_{\gamma\delta}} + \frac{1}{\lambda}\frac{\partial c_1}{\partial F_{\gamma\delta}}\right) \tag{2.45}$$

$$\frac{\partial c_1}{\partial F_{\gamma\delta}} = (j\lambda)^{2/3}\left(\frac{2}{3}\log(j\lambda) + 2\right)T_{\gamma\delta} \tag{2.46}$$

Combining these expressions we obtain the final required derivative.

$$\frac{\partial^2 \lambda}{\partial F_{\alpha\beta}\partial F_{\gamma\delta}} = \frac{D\frac{\partial N_{\alpha\beta}}{\partial F_{\gamma\delta}} - N_{\alpha\beta}\frac{\partial D}{\partial F_{\gamma\delta}}}{D^2} \tag{2.47}$$

2.2. Finite element discretization

The weak form of the governing equations is obtained in the usual manner by multiplication of the strong form equations with admissible test functions, integration over the domain, and application of the divergence theorem. The test functions are denoted $\boldsymbol{w}^u$ and w^d for the linear momentum and phase field equations, respectively. The residual form of the equations for the displacement field, R_u, and phase field, R_d, can then be written as follows where we have omitted any traction boundary conditions.

$$R_u = \int_{\Omega_0} \boldsymbol{P} : \nabla_0 \boldsymbol{w}^u dV = 0 \tag{2.48}$$

$$R_d = \int_{\Omega_0} \left(\frac{\eta}{\Delta t}(d - d_n) w^d + \Psi_c d\, w^d + \Psi_c l_0^2 \nabla_0\, d \cdot \nabla_0 w^d - (1-d)\mathcal{H}\, w^d \right) dV = 0 \tag{2.49}$$

We search for $u_i \in \mathcal{S}_{u_i}$ and $d \in \mathcal{S}_d$ such that Eqs. (2.48) and (2.49) are satisfied $\forall w_i^u \in \mathcal{V}_{w_i^u}$ and $\forall w^d \in \mathcal{V}_{w^d}$ where these function spaces are defined below.

$$\mathcal{S}_{u_i} = \{ u_i \mid u_i \in H^1 \quad u_i = \hat{u}_i \text{ on } \partial\Omega_0^u \} \tag{2.50}$$

$$\mathcal{S}_d = \{ d \mid d \in H^1 \} \tag{2.51}$$

$$\mathcal{V}_{w_i^u} = \{ w_i^u \mid w_i^u \in H^1 \quad w_i^u = 0 \text{ on } \partial\Omega_0^u \} \tag{2.52}$$

$$\mathcal{V}_{w^d} = \{ w^d \mid w^d \in H^1 \} \tag{2.53}$$

Laying the groundwork for the staggered update of the displacement and phase field introduced later, we linearize Eq. (2.48) with respect to $\boldsymbol{u}$ and Eq. (2.49) with respect to d (note that although Eq. (2.49) is already a linear equation in d we update the phase field incrementally in a Newton-like manner).

$$R_u(\boldsymbol{u}^{(k+1)}, d^{(k)}) \approx R_u(\boldsymbol{u}^{(k)}, d^{(k)}) + DR_u(\boldsymbol{u}^{(k)}, d^{(k)})[\delta \boldsymbol{u}] = 0 \tag{2.54}$$

$$R_d(\boldsymbol{u}^{(k+1)}, d^{(k+1)}) \approx R_d(\boldsymbol{u}^{(k)}, d^{(k)}) + DR_d(\boldsymbol{u}^{(k)}, d^{(k)})[\delta d] = 0 \tag{2.55}$$

The directional derivatives above may be expressed as

$$DR_u(\boldsymbol{u}^{(k)}, d^{(k)})[\delta \boldsymbol{u}] = \int_{\Omega_0} \nabla_0 \boldsymbol{w}^u : \mathbb{C} : \nabla_0 \delta \boldsymbol{u}\, dV \tag{2.56}$$

$$DR_d(\boldsymbol{u}^{(k)}, d^{(k)})[\delta d] = \int_{\Omega_0} \left(\left(\Psi_c + \mathcal{H} + \frac{\eta}{\Delta t} \right) \delta d\, w^d + \Psi_c l_0^2 \nabla_0 \delta d \cdot \nabla_0 w^d \right) dV \tag{2.57}$$

where $\mathbb{C}$ is the previously provided fourth order constitutive tensor.

The linearized equations above are then discretized and solved incrementally using the finite element method with appropriately chosen finite dimensional subspaces ($\mathcal{S}_{u_i}^h \subset \mathcal{S}_{u_i}$, $\mathcal{S}_d^h \subset \mathcal{S}_d$, $\mathcal{V}_{w_i^u}^h \subset \mathcal{V}_{w_i^u}$, $\mathcal{V}_{w^d}^h \subset \mathcal{V}_{w^d}$). The 2D domain is partitioned using 4-node quadrilateral elements and the typical bilinear Lagrange basis functions are used for the test and trial spaces, consistent with the standard Galerkin formulation. We represent these field approximations with the shape function matrices, $\boldsymbol{N^u}$ and $\boldsymbol{N}^d$, for the displacement and phase field, respectively. The corresponding matrices of shape function gradients are represented analogously by $\boldsymbol{B^u}$ and $\boldsymbol{B}^d$.

$$\begin{array}{ll} \boldsymbol{u} \approx \boldsymbol{u}^h = \boldsymbol{N^u}\bar{\boldsymbol{u}} & d \approx d^h = \boldsymbol{N}^d \bar{\boldsymbol{d}} \\ \delta \boldsymbol{u} \approx \delta \boldsymbol{u}^h = \boldsymbol{N^u} \delta \bar{\boldsymbol{u}} & \delta d \approx \delta d^h = \boldsymbol{N}^d \delta \bar{\boldsymbol{d}} \\ \boldsymbol{w}^u \approx \boldsymbol{w}^{u^h} = \boldsymbol{N^u} \bar{\boldsymbol{w}}^u & w^d \approx w^{d^h} = \boldsymbol{N}^d \bar{\boldsymbol{w}}^d \end{array}$$

Substituting these approximations along with their gradients into Eqs. (2.54) and (2.55), and invoking the arbitrariness of the vectors $\bar{\boldsymbol{w}}^u$ and $\bar{\boldsymbol{w}}^d$, we can identify the discrete elemental residual vectors and jacobian matrices,

$$\boldsymbol{R}_{\bar{\boldsymbol{u}}}^{e(k)} = \int_{\Omega_0} \boldsymbol{P}^{(k)} : \boldsymbol{B^u}\, dV = \boldsymbol{0} \tag{2.58}$$

$$\boldsymbol{J}_{\bar{\boldsymbol{u}}}^{e(k)} = \int_{\Omega_0} \boldsymbol{B^u} : \mathbb{C}^{(k)} : \boldsymbol{B^u}\, dV \tag{2.59}$$

$$\boldsymbol{R}_{\bar{\boldsymbol{d}}}^{e(k)} = \int_{\Omega_0} \left(\Psi_c \left(\boldsymbol{N}^{d^T} \boldsymbol{N}^d + l_0^2 \boldsymbol{B}^{d^T} \boldsymbol{B}^d \right) \bar{\boldsymbol{d}}^{(k)} \right) dV + \int_{\Omega_0} \frac{\eta}{\Delta t} \boldsymbol{N}^{d^T} \boldsymbol{N}^d \left(\bar{\boldsymbol{d}}^{(k)} - \bar{\boldsymbol{d}}_n \right) dV - \int_{\Omega_0} (1 - \boldsymbol{N}^d \bar{\boldsymbol{d}}^{(k)}) \boldsymbol{N}^{d^T} \mathcal{H}\, dV = \boldsymbol{0} \tag{2.60}$$

$$\boldsymbol{J}_{\bar{\boldsymbol{d}}}^{e(k)} = \int_{\Omega_0} \left(\left(\Psi_c + \mathcal{H} + \frac{\eta}{\Delta t} \right) \boldsymbol{N}^{d^T} \boldsymbol{N}^d + \Psi_c l_0^2 \boldsymbol{B}^{d^T} \boldsymbol{B}^d \right) dV \tag{2.61}$$

where the e superscript signifies elemental quantities and the operation $\boldsymbol{A}$: $\boldsymbol{B}$ represents the double contraction of tensors $\boldsymbol{A}$ and $\boldsymbol{B}$. Additionally, the $(\ \cdot\ )^{(k)}$ notation implies that the quantity $(\ \cdot\ )$ is evaluated using the relevant field variables at iteration k. The elemental quantities are then assembled into the global residual vectors and jacobian matrices via the standard finite element assembly operators.

$$\boldsymbol{R}_{\bar{\boldsymbol{u}}}^{(k)} = \mathcal{A}_{e=1}^{N_{elem}} \boldsymbol{R}_{\bar{\boldsymbol{u}}}^{e(k)} \quad \boldsymbol{J}_{\bar{\boldsymbol{u}}}^{(k)} = \mathcal{A}_{e=1}^{N_{elem}} \boldsymbol{J}_{\bar{\boldsymbol{u}}}^{e(k)} \tag{2.62}$$

$$\boldsymbol{R}_{\bar{\boldsymbol{d}}}^{(k)} = \mathcal{A}_{e=1}^{N_{elem}} \boldsymbol{R}_{\bar{\boldsymbol{d}}}^{e(k)} \quad \boldsymbol{J}_{\bar{\boldsymbol{d}}}^{(k)} = \mathcal{A}_{e=1}^{N_{elem}} \boldsymbol{J}_{\bar{\boldsymbol{d}}}^{e(k)} \tag{2.63}$$

These global quantities are then used separately to compute the Newton-type correction of the displacement and phase field nodal variables.

$$\bar{\boldsymbol{u}}^{(k+1)} = \bar{\boldsymbol{u}}^{(k)} - \boldsymbol{J}_{\bar{\boldsymbol{u}}}^{(k)^{-1}} \boldsymbol{R}_{\bar{\boldsymbol{u}}}^{(k)} \tag{2.64}$$

$$\bar{\boldsymbol{d}}^{(k+1)} = \bar{\boldsymbol{d}}^{(k)} - \boldsymbol{J}_{\bar{\boldsymbol{d}}}^{(k)^{-1}} \boldsymbol{R}_{\bar{\boldsymbol{d}}}^{(k)} \tag{2.65}$$

Algorithm 1 provides the details of the iterative staggered solution used herein. Note that this scheme is essentially

Algorithm 1 Staggered update of nodal degrees of freedom, $(\bar{\boldsymbol{u}}, \bar{\boldsymbol{d}})$.

```
t ← 0
ū, d̄ ← 0
while t < t_final do
    t ← t + Δt
    û ← t · û_final {Update prescribed displacements}
    k ← 0
    while ||R_ū^(k)||_2 / ||R_ū^(0)||_2 > 10^−8 do
        k ← k + 1
        Update ū via Equation 2.64
    end while
    Update ℋ with updated ū
    k ← 0
    while ||R_d̄^(k)||_2 / ||R_d̄^(0)||_2 > 10^−8 do
        k ← k + 1
        Update d̄ via Equation 2.65
    end while
end while
```

identical to that of Miehe et al. (2010a). Sufficiently small applied displacement increments are chosen such that the results are indistinguishable under further reduced load incrementation. During crack propagation the displacement increment is significantly reduced from an initial value of approximately 10^{-4} $[mm]$ to a value of 10^{-6} $[mm]$. We also note the use of a backtracking line search that is employed occasionally during the displacement update in order to ensure the determinant of the deformation gradient (J) is strictly positive at all quadrature points in the discretized domain. If this requirement is violated following an update of the displacement field, the newton increment, $\delta \boldsymbol{u}$, is reduced by a constant multiplier, $0 < \gamma < 1$, until the condition is satisfied. Subsequently, the displacement newton iteration is allowed to continue to convergence. Although this procedure is rarely required, it has proven to be an effective strategy for delaying failure of the numerical simulations in certain instances. The jacobian and residual equations are integrated using a standard 4-point Gauss quadrature rule for a quadrilateral element and the irreversibility requirement is enforced via a history variable stored at each quadrature point.

3. Numerical and experimental methods

3.1. Design of the composite samples

In this section we outline the process used to study the failure mechanism of 3D-printed polymer composites undergoing large deformation both experimentally and numerically. A specific parameterized geometry is proposed in order to study

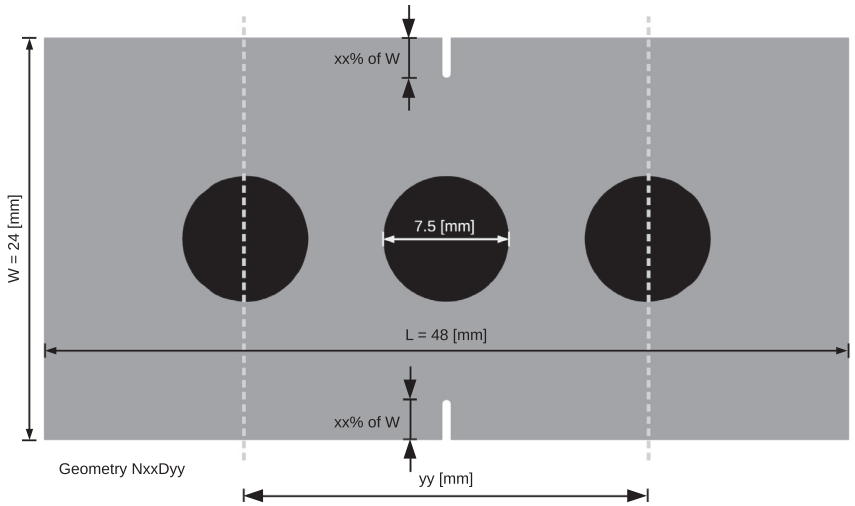


Fig. 2. Geometric parameterization, NxxDyy, in which xx and yy are illustrated graphically.

this behavior which consists of a soft matrix, within which three stiff circular inclusions are embedded as shown in Fig. 2. Additionally, two notches of various lengths are introduced in the middle of the specimen. By varying the distance between stiff inclusions and the notch lengths, we are able to alter the failure sequence.

In total, 9 different geometries (3 initial notch lengths and 3 distances between inclusions) are subjected to uniaxial tension until complete failure of the specimen. We adopt the short notation N__D__ to describe the geometry of the specimens that reflects the notch length as well as spacing between rigid inclusions. For instance, the notation N05D18 corresponds to a specimen with an 18 $[mm]$ distance between inclusion centers and an initial notch length corresponding to 5% of the total specimen width. This is illustrated graphically in Fig. 2, below. Note that the out-of-plane thickness of all samples is 2.5 $[mm]$.

3.2. Experimental testing

The composite specimens with the selected geometries (see Fig. 2) were produced by multimaterial PolyJet 3D-printing using a Stratasys Object Connex 3 printer that supports fabrication of specimens containing up to 3 materials simultaneously. The matrix of the composite was printed using soft elastomeric TangoBlackPlus material (TP), while stiff VeroWhite (VW) material was selected for the inclusions. The printed specimens were subjected to uniaxial tension using the universal testing machine Shimadzu EZ-LX with a low strain rate of 10 mm/min to avoid dynamic effects and decrease the influence of rate-dependent TP material behavior. For consistency all samples were printed with the same orientation in the building tray, even though supplementary tests verified that the printing orientation has only minor effect on the failure behavior. The deformation process was captured using a CMOS camera, enabling the use of digital image correlation (DIC) to estimate the strain field within the soft matrix prior to crack initiation.

3.3. Numerical investigation

The numerical formulation was implemented using the open-source, C++ finite element library, deal.II Arndt et al. (2019), and PETSc (Balay et al., 2019) for parallel, sparse linear algebra. First, the elastic parameters for the soft TP material were estimated from select homogeneous uniaxial tension experiments. Near incompressibility was assumed and the bulk modulus was taken to be 100 times the calibrated shear modulus of 0.24 $[MPa]$, resulting in an initial Poisson's ratio of approximately 0.495. These are consistent with previously reported material parameters (Slesarenko and Rudykh, 2018). The stiff VW inclusions may effectively be regarded as rigid due to their high stiffness relative to TP. The elastic modulus as reported on the manufacturer's data sheet (ver, 2018) is in the range $2,000 - 3,000$ $[MPa]$. For the purpose of the numerical studies presented herein, we assume the material has an approximate Poisson's ratio of 0.4. Using the lower bound on the elastic modulus from the manufacturer we estimate the shear modulus of the rigid material to be 714 $[MPa]$ and bulk modulus to be 3.33 $[GPa]$, based on the standard theory of isotropic, linear elasticity (i.e. $\mu = E/(2(1+\nu))$ and $\kappa = E/(3(1-2\nu))$). The finite element size is approximately $l_0/6$ in all regions in which cracks may nucleate or propagate and the boundary conditions are illustrated in Fig. 3 below. Note that in order to obtain numerical predictions more consistent with experiments, we break the symmetry about the vertical axis by applying a small shift of the center inclusion (0.1% of the specimen width). This 0.024 $[mm]$ shift is less than the 0.1 $[mm]$ "accuracy" asserted by the manufacturer (pol, 2018) and the 0.03 $[mm]$ layer thickness.

The material parameters used in subsequent numerical analyses are provided in Table 1. In this work, rather than employing a complex calibration procedure for the phase field model parameters, we set the length scale parameter as small

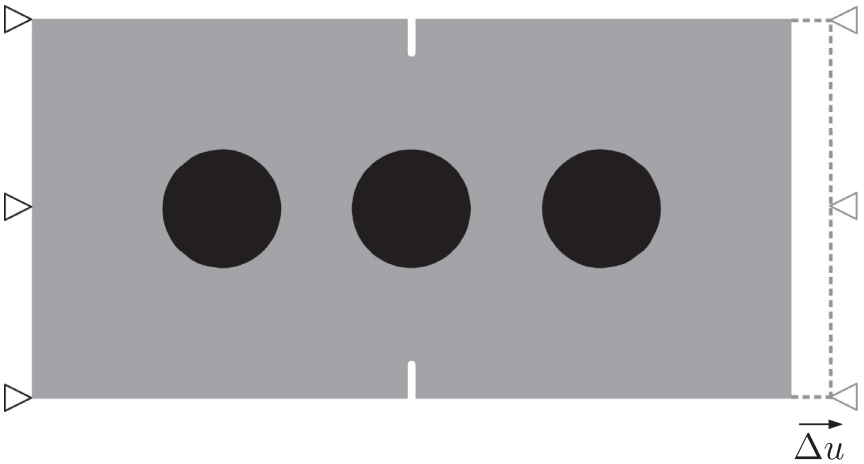


Fig. 3. Boundary conditions imposed in numerical simulations. The left edge is fixed while a displacement is applied to the right edge.

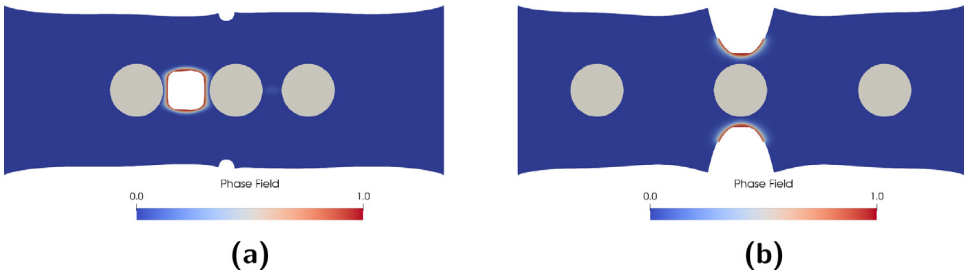


Fig. 4. Predicted crack initiation comparison for (a) N05D18 and (b) N20D30. Note that the plots are clipped at a phase field value of 0.95.

Table 1
Material parameters.

	κ [MPa]	μ [MPa]	l_0 [mm]	Ψ_c [$\frac{N \cdot mm}{mm^3}$]
TangoBlackPlus	24	0.24	0.5	0.34
VeroWhite	3,330	714	0.5	1.05

as possible based on computational limitations ($l_0 = 0.5$ *mm* similar to the 0.5504 *mm* obtained for a rubber material by Loew et al. (2019)) and adjust the critical energy density ($\Psi_c = 0.34$ $\frac{N}{mm^2}$) in order to approximately match the failure stretch of only one (i.e. the N10D24) experiment. The resulting parameter set gave reasonably predictive results for the other experiments with different geometries. The same length scale parameter is used for the stiff inclusions and the critical energy density is estimated using the approximation $\Psi_c = \sigma_c^2/(2E)$ with a critical stress of 65 *MPa* (corresponding to the tensile strength estimated by the manufacturer). Note that since the stiff inclusions are not directly loaded, the strain energy density of the inclusion material never exceeds the critical threshold and consequently has little to no effect on the numerical predictions. In the future, a more complex calibration procedure such as the one outlined in Loew et al. (2019) may be employed. Furthermore, future studies introducing stochasticity may be conducted in order to identify the material parameters (see Rappel et al. (2019) for example) and better understand the effect of uncertainty in their value (see Hauseux et al. (2018) for an example regarding hyperelasticity).

Multiple simulations were performed corresponding to the experimentally tested geometric configurations. For particular combinations of the initial notch length and distance between inclusions, cracks initiate either between inclusions or at the notch tip as illustrated in Fig. 4. Here we note that when cracks initiate near the rigid inclusion pole rather than at the notch tip, this is likely related to cavitation resulting from the stress triaxiality as is discussed in Volokh and Aboudi (2016). The relationship between this phenomenon and fracture has also been recently investigated by Raayai-Ardakani et al. (2019). Additionally, it should be mentioned that due to the large stretch ratios that soft materials generally exhibit prior to failure, stress concentrators such as notches are typically significantly blunted. This generally results in lower sensitivity to notches when compared with materials that are significantly stiffer. Nonetheless, our numerical/experimental results do indicate that a sufficiently large notch will indeed lead to crack initiation at the notch tip.

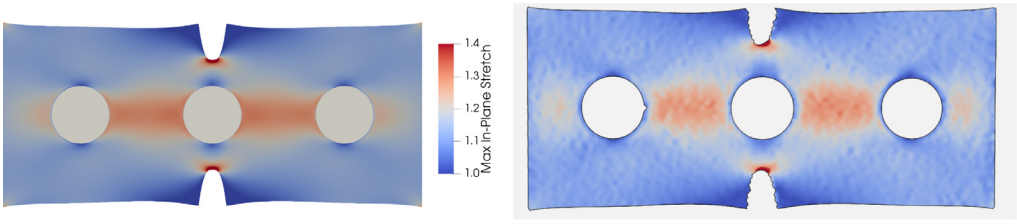


Fig. 5. Stretch comparison for N20D30 at a prescribed end-displacement of 6.6mm compared with DIC image.

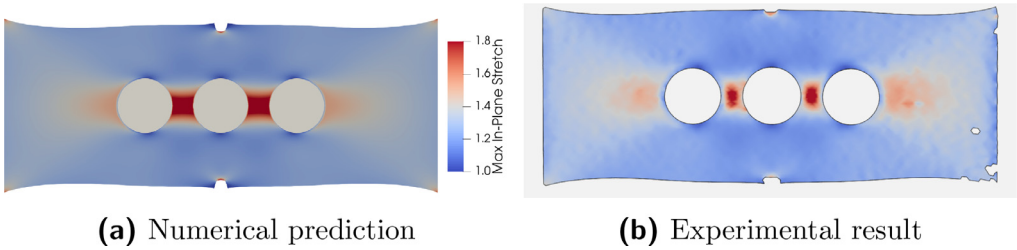


Fig. 6. Stretch comparison for N05D18 at a prescribed end-displacement of 11.8mm compared with DIC image.

3.4. Pre-fracture strain field comparison

In order to validate the employed elastic strain energy density, we compare the calculated strain field in the specimen before fracture with the strain field observed experimentally using DIC. As illustrated in Fig. 5 for specimen N20D30, the strain localization is observed between inclusions as well as near the initial notch tip, both numerically and experimentally. However, in specimen N05D18 the strain primarily localizes between inclusions rather than near the notch tip (Fig. 6). A minor difference between the numerically-estimated and experimentally-observed strain fields occurs near the boundary of the rigid inclusions (compare Fig. 6 (a) and (b)). This phenomenon may be attributed to the actual non-uniform out-of-plane deformation near the rigid inclusions, which may not be accurately captured by the employed plane stress numerical approximation (see Appendix A). Note that we do not use the data obtained by DIC for model calibration. See Loew et al. (2019) for an example where DIC data is used in conjunction with force-displacement results in order to calibrate the fracture parameters of the model.

4. Numerical and experimental studies

In this section we investigate the effects of the initial notch length and distance between inclusions on the failure pattern of the polymer composites, both numerically and experimentally. First, we compare the qualitative failure pattern via a side-by-side comparison of failure sequences for a few representative geometries in Section 4.1. Second, we provide the force versus displacement curves for comparison in Section 4.2, and an illustration of the numerically and experimentally computed external work to failure is provided in Section 4.3.

4.1. Failure sequence comparisons

First, we provide a qualitative comparison of the experimental and numerical failure patterns for a few representative geometries. For the samples with the largest distance between inclusions ($D = 30$ $[mm]$) and both the smallest (N05D30 in Fig. 7) and the largest (N20D30 in Fig. 8) initial notch lengths, it is clear that the fracture nucleates at the notch tip. This indicates that the inclusions are a sufficient distance apart to prevent substantial elastic energy accumulation between inclusions with respect to the elastic energy accumulated near the notch tip. In both cases it is observed that once the initial crack is arrested by the center inclusion, a secondary fracture surface nucleates between inclusions. In the case of N05D30, it is observed that although the initial crack has begun propagating around the center inclusion, Fig. 7(f) shows the nucleation of new fracture surface on both the left and right side of the inclusion. It is interesting that the initiation of new fracture surface on both sides of the center inclusion is also predicted numerically (see Fig. 7(e)).

In the case of the larger initial notch length corresponding to the N20D30 geometry, Fig. 8(f) shows a secondary crack initiation more clearly since we experimentally observe the initial cracks do not begin propagating around the center inclusion before the secondary crack initiates and propagates. In contrast with N05D30, Fig. 8(e) shows secondary crack initiation on only one side of the center inclusion in somewhat remarkable correspondence with the experimental observation in Fig. 8(f). A very similar pattern is observed for the N20D24 geometry with the same initial notch length and smaller dis-

tance between inclusions. Fig. 9 illustrates the initial fracture surface nucleation and propagation from the notch tip, with subsequent nucleation and propagation of a secondary crack on only one side of the center inclusion.

Once the inclusions are sufficiently close together cracks typically initiate between the inclusions rather than at the initial notch tip. Fig. 10 illustrates the failure sequence for the N10D18 geometry. It is interesting to note that the phase field formulation is capable of capturing not only the location of initiation of the first crack, but also the subsequent mild crack evolution at the notch tip as shown in Fig. 10(e) and (f). Note that this mild secondary initiation does not occur for the N05D18 geometry with smaller initial notch length as illustrated in Fig. 11. Additionally, we note that while the sequences shown in Figs. 7 and 10 generally exhibit failure at similar global stretch values ($\Lambda = \frac{\text{current length}}{\text{initial length}}$), for other samples we do not have ideal agreement between experiments and simulations with respect to the global stretch values (although we do have a nearly perfect qualitative match). In general, this discrepancy is expected due to the complexity of the TP material properties and/or inconsistency in the 3D-printing process (factors that may not be sufficient to describe using the single failure parameter of the employed numerical model). Nevertheless, very good agreement between the experimen-

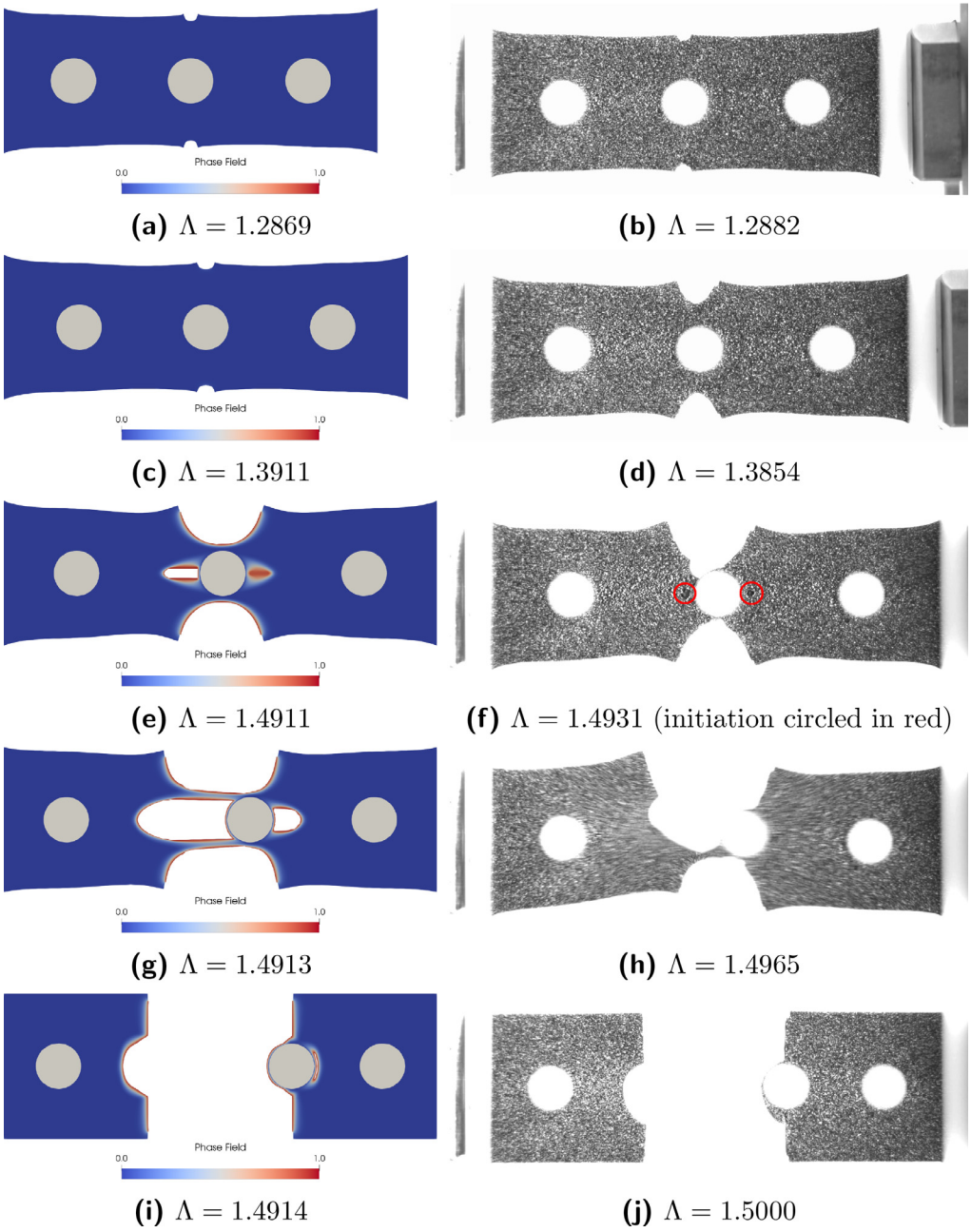


Fig. 7. N05D30 crack initiation sequence at different values of global stretch, Λ. Numerical results (left column) and experimental results (right column).

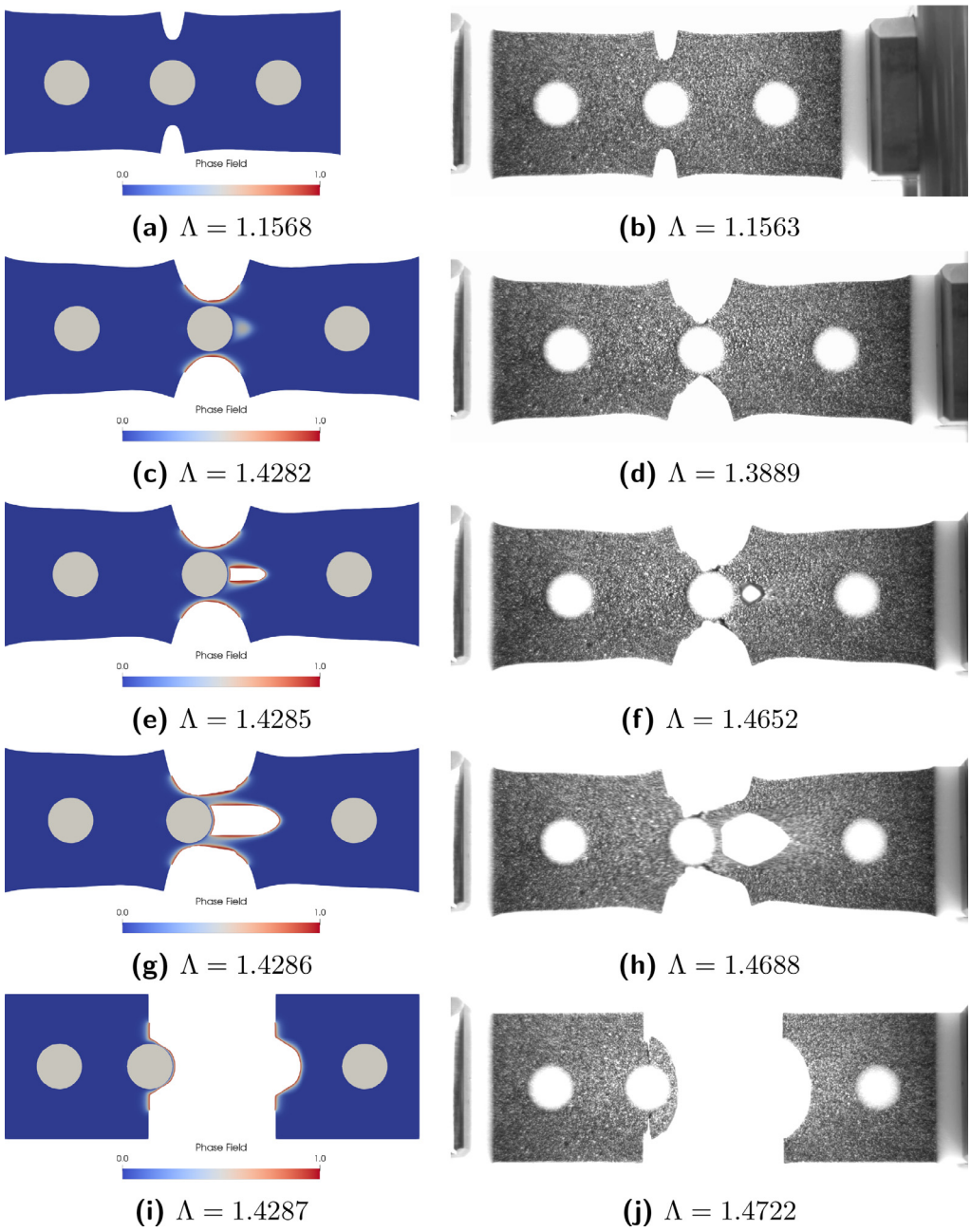


Fig. 8. N20D30 crack initiation sequence at different values of global stretch, Λ. Numerical results (left column) and experimental results (right column).

tally observed failure sequences and numerical predictions once again illustrates the promising capability of the proposed formulation to assess the overall fracture behavior of the 3D-printed composites undergoing large deformations.

4.2. Force versus displacement response

While in the previous section we focus on the qualitative failure behavior of the 3D-printed composites, here we examine the quantitative prediction via force-displacement curves. Fig. 12 illustrates the experimental curves and corresponding numerical predictions (note that only one experiment for each geometry is shown for clarity). It is clear that an increase in the notch length leads to the slight decrease in the effective structural stiffness and a decrease in the critical strain at which crack initiation and subsequent catastrophic failure occur. This trend is also confirmed by the numerical simulations for all geometries irrespective of the distance between inclusions. Comparison between corresponding experimental and numerical data reveals very good agreement while the structures are loaded elastically, although minor under-prediction of the struc-

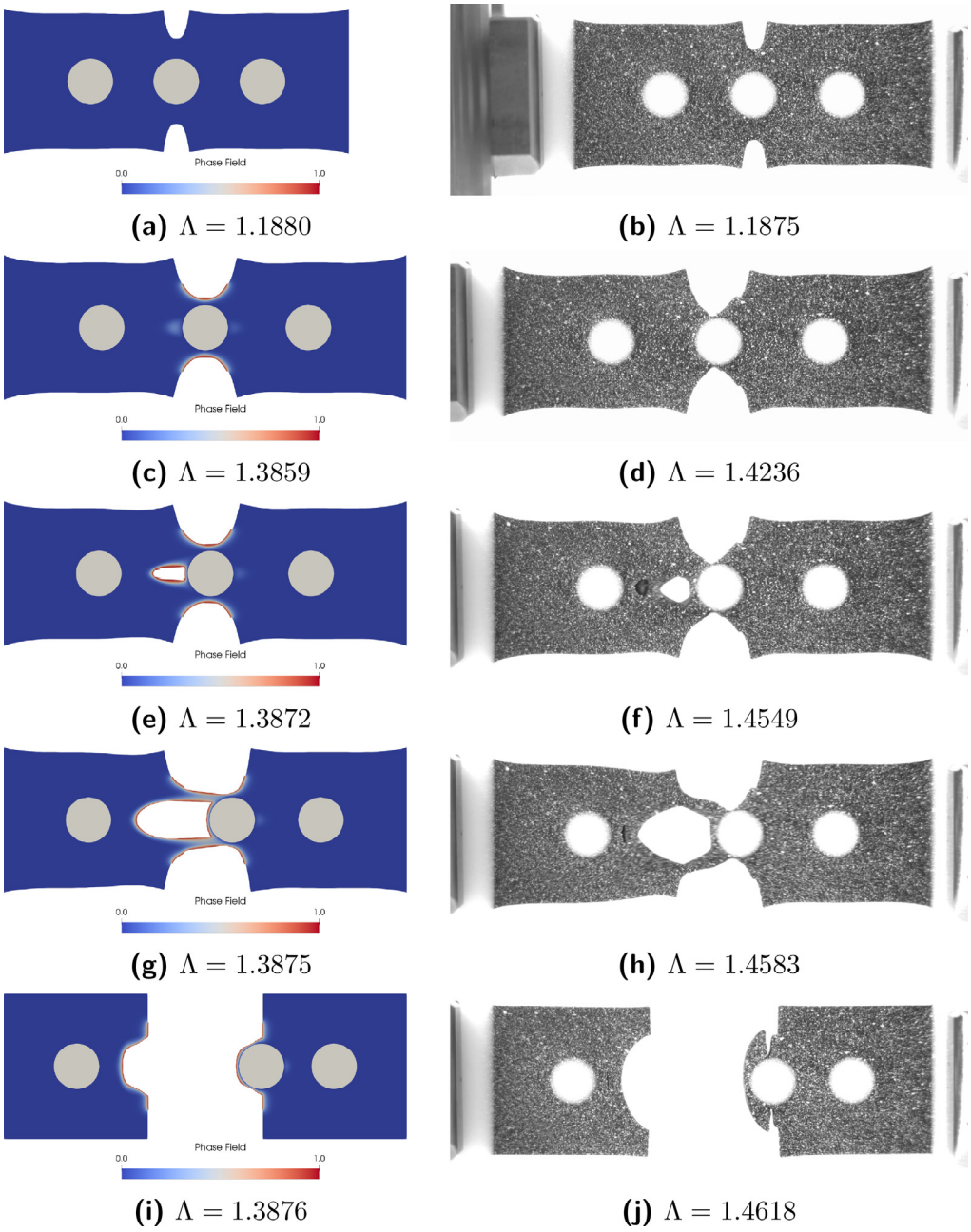


Fig. 9. N20D24 crack initiation sequence at different values of global stretch, Λ. Numerical results (left column) and experimental results (right column).

tural stiffness is observed when the inclusions are closest together (corresponding to $D = 18$ $[mm]$). This can be explained by the absence of the out-of-plane stiffening effect near the rigid inclusions in the proposed plane stress formulation (see Appendix A).

Discrepancies are observed between experimental and numerical force-displacement curves only after crack initiation. As mentioned in the previous section, this is expected due to the very complex behavior of the soft 3D-printed material during failure. While the numerical prediction is not perfect, it is still fascinating that the numerical model with its simplifying assumptions (e.g. quasi-static, isotropic, rate-independent hyperelastic model in plane stress with a single numerical failure parameter, Ψ_c) is capable of qualitatively describing the failure behavior of the considered composite structures. For instance, we observe the force decrease due to crack initiation and subsequent force increase after crack arrest both numerically and experimentally when the inclusions are sufficiently far apart (e.g. $D = 30$ $[mm]$). Furthermore, the specimens in which the inclusions are closest together ($D = 18$ $[mm]$) fail catastrophically without crack arrest. Recall that in the former case cracks initially nucleate at the notch tip, while in the latter case cracks nucleate between the inclusions and exhibit

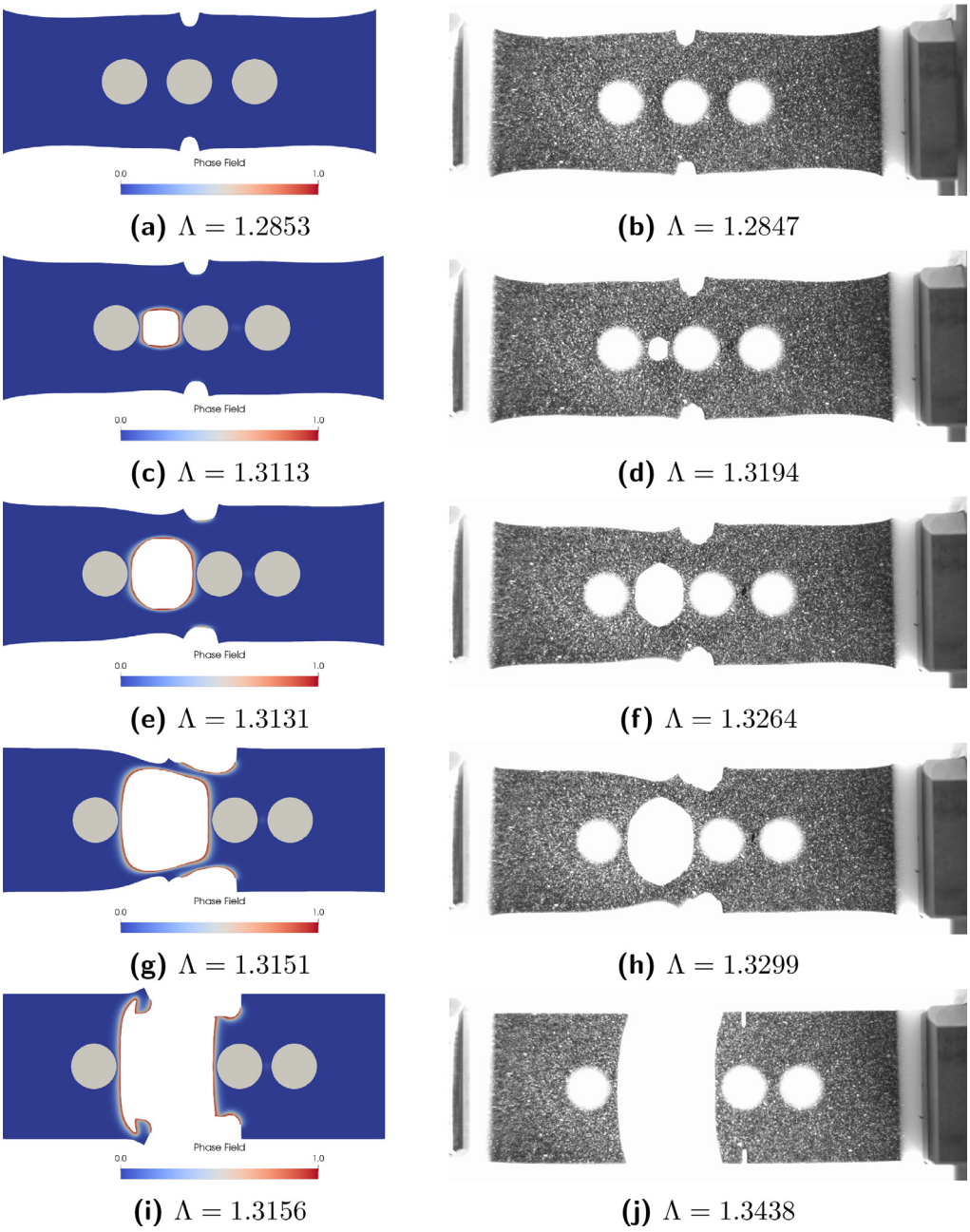


Fig. 10. N10D18 crack initiation sequence at different values of global stretch, Λ. Numerical results (left column) and experimental results (right column).

fast subsequent crack propagation. These phenomena are illustrated briefly in Appendix B, while the numerically predicted crack initiation behavior at the notch tip is also briefly investigated in Appendix C through comparison with contour integral calculations.

In Fig. 13 below, we present the numerically predicted force versus displacement curves grouped by notch length where we have included the numerical prediction for the homogeneous material without inclusions for comparison. For completeness, additional numerical simulations were performed using an initial notch length corresponding to 15% of the total width (i.e. N15D__), a distance between inclusions of 21 [*mm*] (i.e. N__D21), and 27 [*mm*] (i.e. N__D27) for a total of 20 numerically obtained values. In addition, the peak forces for each notch length are illustrated in Fig. 14(a) along with the predicted results for the homogeneous case. It is clearly observed that for N10, N15, and N20 the inclusions provide a significant increase in strength (peak force) irrespective of the distances between the inclusions studied herein. However, the situation is quite different for the shortest notch length N05 in which the inclusions must be sufficiently far apart in order to obtain an increase in strength when compared to the pure polymer case. We also note the presence of the local maximum for

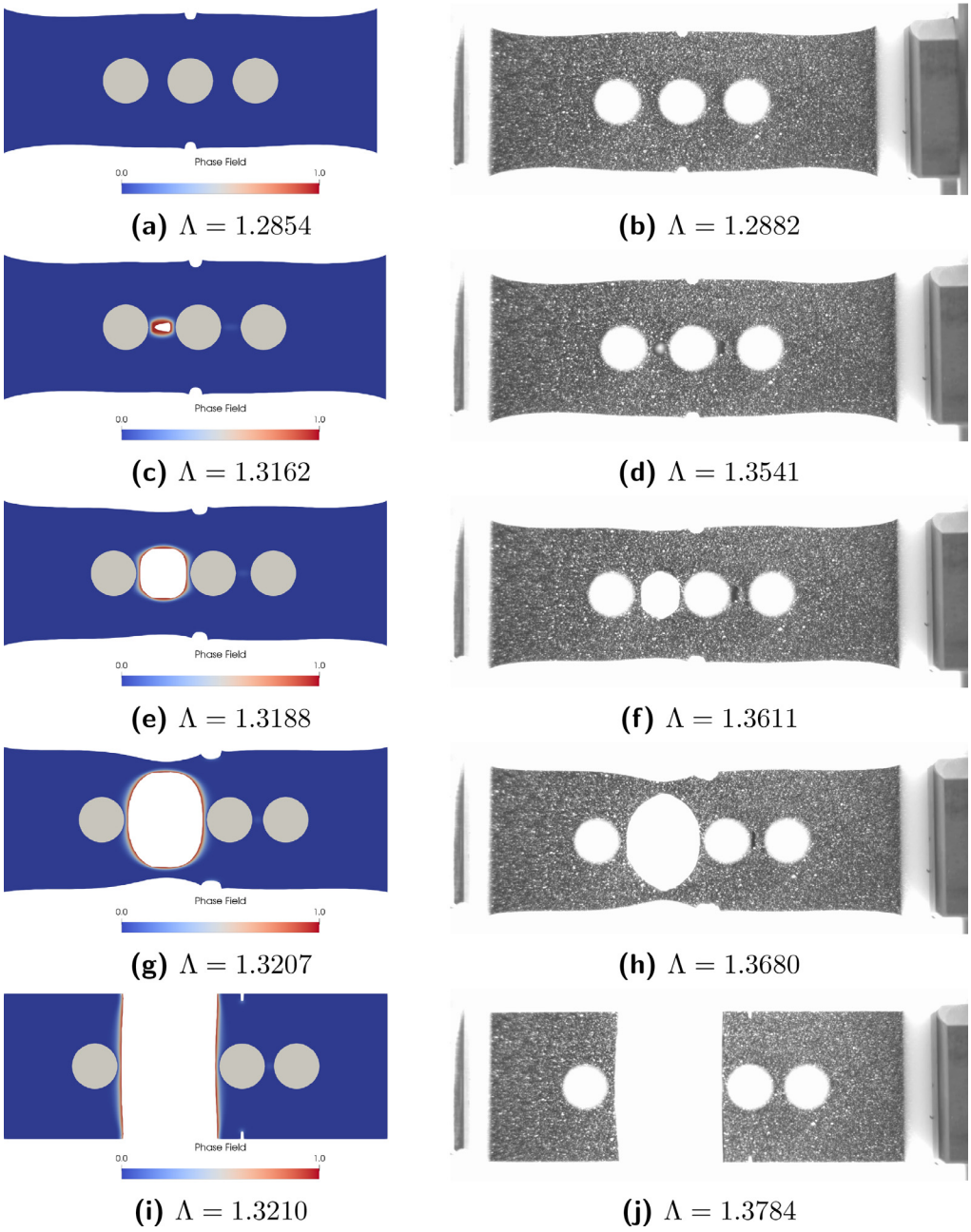


Fig. 11. N05D18 crack initiation sequence at different values of global stretch, Λ. Numerical results (left column) and experimental results (right column).

the N05 case which suggests that there is an optimal distance between inclusions that will maximize the strength. Spacing the inclusions closely together (e.g. $D = 18$) in this case clearly results in worse performance when compared to the homogeneous result. Finally, we highlight the fact that the addition of the rigid inclusions, when appropriately spaced, seem to also increase the structural failure stretch in all cases except for N05 where the is a marginal improvement when compared with N05D27. This is quite an interesting result since it is not unusual for the failure stretch to decrease with the addition of rigid particles (see Wu et al. (2016) for instance).

4.3. External work comparison

While comparison between the failure sequences and force-displacement curves provides important insight into the behavior of proposed composite structures, we also provide the external work to failure as an additional quantitative measure for comparison. The external work to failure is computed via numerical integration of the force versus displacement curves

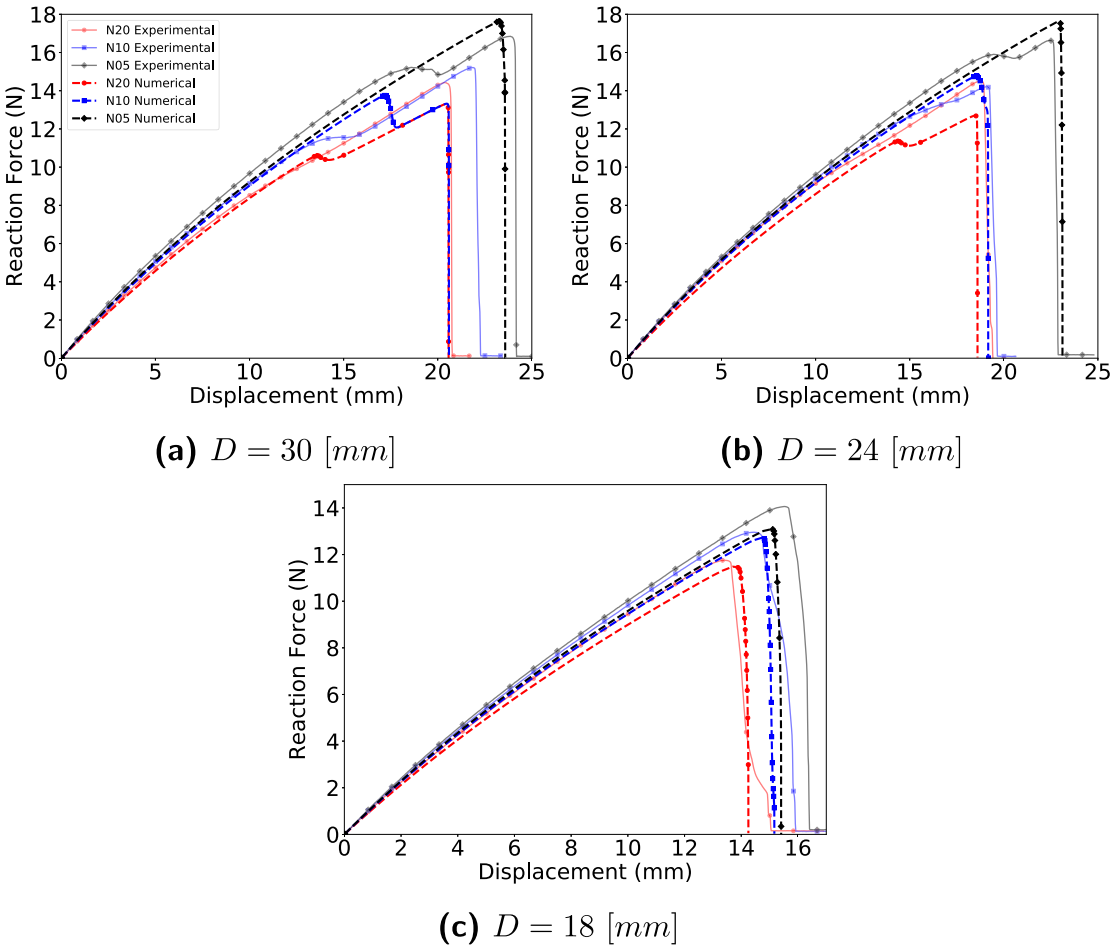


Fig. 12. Experimental and numerical force versus displacement curves grouped by the geometric distance between inclusions (D).

presented in the previous section. Fig. 15 below provides a simple visual comparison of the numerically and experimentally obtained external work.

Here we highlight the non-trivial appearance of a local maximum between N05D24 and N05D30. This likely occurs due to the approximate equality between the inclusion spacing and the space between outer inclusions and the rigid boundary for sample N05D27, which may contribute to the external work increase as a result of the more “uniform” load distribution in the soft matrix. We note this in addition to the peculiar shape of the surface near N10D21 where numerically we observe a deviation from the general trend. This deviation occurs during the transition between cracks nucleating at the initial notch tip and cracks initiating between inclusions. The N10D21 geometry results in predicted cracks initiating at both the initial notch tip and between inclusions, seemingly simultaneously. This simultaneous initiation of multiple cracks leads to the increase in the displacement required to finally separate the structure, which results in additional area under the force-displacement curve. Consistent with previously presented results, we see that the numerical model is capable of capturing the general trend of the experimental results.

The numerically predicted external work versus distance between inclusions is presented in Fig. 14(b) along with the prediction for the homogeneous case without inclusions. In this figure we see the toughening effect explicitly associated with the addition of the rigid inclusions (i.e. the potential increase in external work required for complete structural failure resulting from the inclusion addition). However, for both the N05 and N10 cases the situation is not very straight-forward since there appears to be a minimum distance between inclusions in order to improve this measure of structural toughness. This is likely also true for the N15 and N20 cases but not for the range of distances between inclusions that we have studied herein (if one extrapolates the curves from $D = 18$ to $D = 16$ they would likely intersect the pure polymer case as well). Also, the appearance of the local maxima for the N05 and N10 cases clearly demonstrates that the optimal inclusion spacing for structural toughness is not a trivial matter. However, the curves do clearly show that spacing the inclusions too close together can certainly have a negative impact on the structure’s mechanical performance.

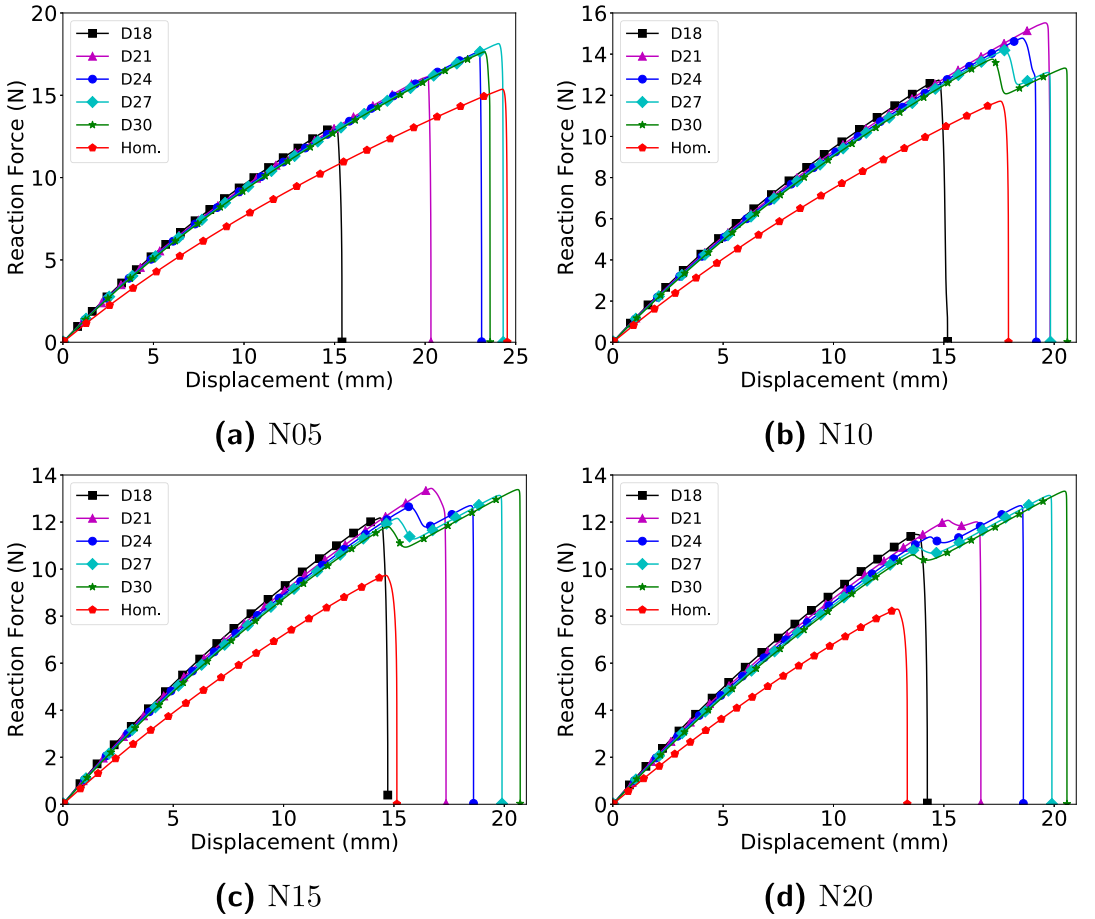


Fig. 13. Numerical force versus displacement curves grouped by notch length along with the numerical prediction for the homogeneous case without inclusions for comparison.

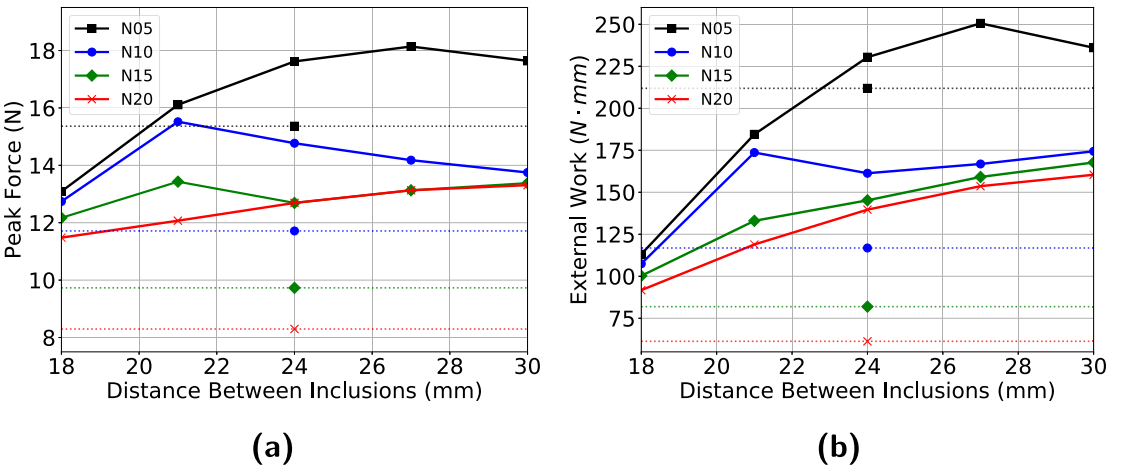


Fig. 14. Numerically predicted (a) peak forces and (b) external work versus distance between inclusions for each notch length. Additionally, a horizontal dotted line (with marker style of the corresponding notch length) signifies the predicted value for the homogeneous case without inclusions. Figure (b) is discussed in the following subsection but placed alongside (a) for ease of comparison.

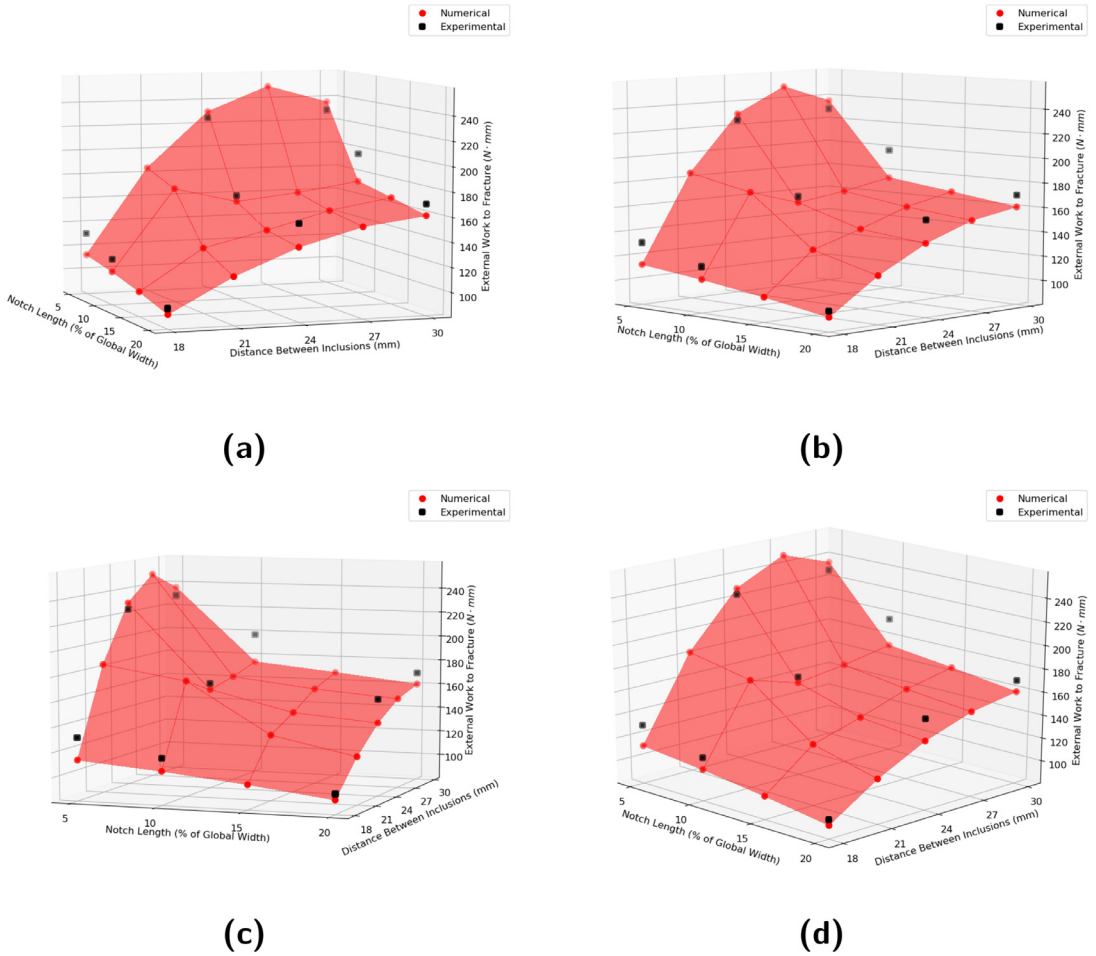


Fig. 15. The numerically computed external work surface viewed from various angles along with the relevant experimentally computed data points.

5. Concluding remarks

In this work we investigate the failure of 3D-printed polymer composites comprised of a soft matrix with stiff inclusions. The composites are fabricated through multimaterial 3D-printing and uniaxial tests are performed to investigate their mechanical behavior and failure mechanisms. In order to obtain a more detailed picture of the underlying physics, we numerically simulate the failure of the composite structures using the phase field fracture method with an energetic threshold using an efficient plane-stress formulation. The two-dimensional numerical formulation is provided and the reduced consistent tangent tensor is analytically derived.

It is demonstrated, both experimentally and numerically, that changes in particular geometric parameters (e.g. inclusion spacing and initial notch length) have a strong impact on the resulting failure sequence and overall structural resistance to failure. Although the numerical model is derived with several simplifying assumptions, the results demonstrate that it is capable of capturing the complex large deformation failure sequences of the 3D-printed composite structure presented herein. This includes a non-trivial secondary crack initiation and propagation in the bulk material consistent with the corresponding experimental observations.

Additionally we highlight an interesting behavior of the structures studied herein that is of practical interest. We have observed that the addition of stiff inclusions results in an expected improvement in the structure's mechanical properties (namely, the strength, toughness, and stiffness). However, the situation is not as obvious as one might expect. Spacing the inclusions too closely can clearly result in a degradation of structural strength and toughness. This has been demonstrated both experimentally and numerically. Not only does there appear to be a minimum inclusion spacing to be effective with respect to the homogeneous matrix case, but we have also numerically observed an optimal inclusion spacing which maximizes the structural strength and toughness (this is most clearly observed for the case with the shortest initial notch length).

Finally, we acknowledge that rate-dependent effects may be significant during crack propagation and their inclusion may improve the accuracy of the predictions. Future numerical and experimental study should elaborate on the observed failure behavior by considering more complex geometries while taking into account the viscous behavior of th e material.

CRediT authorship contribution statement

Jonathan Russ: Conceptualization, Methodology, Software, Writing - original draft. **Viacheslav Slesarenko:** Conceptualization, Investigation, Writing - original draft. **Stephan Rudykh:** Conceptualization, Writing - review & editing. **Haim Waisman:** Conceptualization, Writing - review & editing.

Acknowledgements

The support by MOT/CAA of Israel is gratefully acknowledged.

Appendix A. Validation of plane stress approximation

In an effort to validate the choice of a plane stress assumption versus the alternative plane strain assumption in two space dimensions, we provide numerical evidence with a single representative geometry investigated in this work.

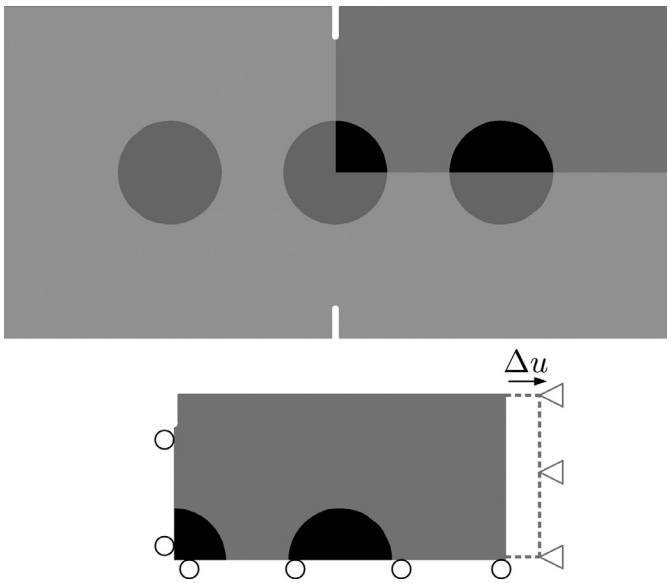


Fig. A.16. Boundary conditions for plane stress validation problem.

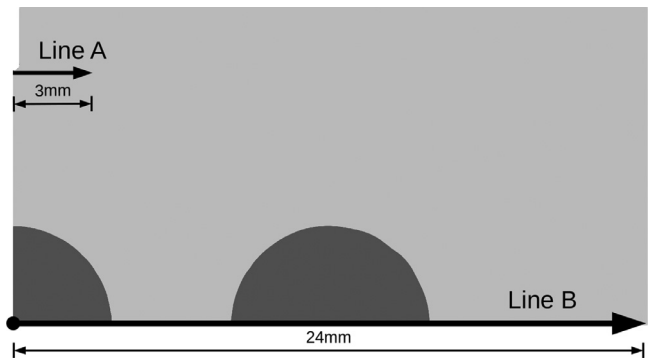


Fig. A.17. Lines along which the strain energy density is compared. In three-dimensions the lines lie in the plane at the center of the out-of-plane thickness.

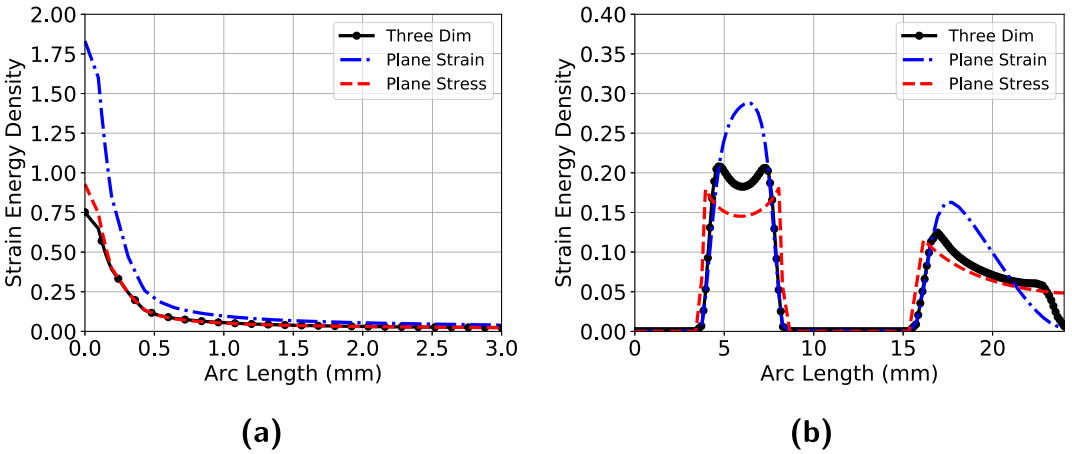


Fig. A.18. Line plots of strain energy density along (a) Line A and (b) Line B as illustrated in Fig. A.17.

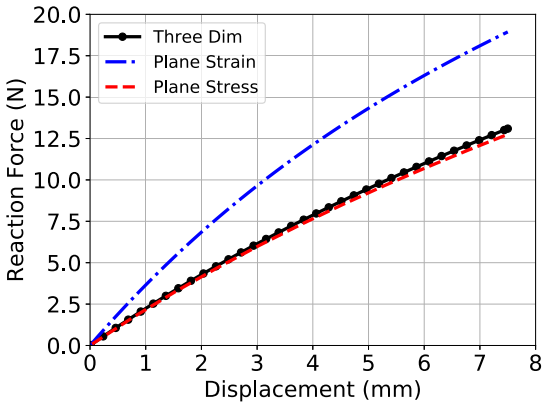


Fig. A.19. Force vs. displacement curves illustrating the consistency of the plane stress approximation with that of the three-dimensional formulation.

Numerical simulations without the phase field fracture physics were performed utilizing the plane stress assumption, a plane strain formulation, and the full three-dimensional representation. The plane strain and three-dimensional simulations were performed using exactly the same form of strain energy density used in this work (namely, Eq. (2.7)) and volumetric-locking is alleviated using a standard mean-dilatation formulation consistent with Bonet and Wood (2008). For the three-dimensional analyses, we use a standard 8-node hexahedral element with tri-linear Lagrange shape functions. An identical in-plane mesh is created for all three cases and the three-dimensional mesh is created by extruding this two-dimensional mesh in the out-of-plane direction with 6 elements through the specimen thickness. We choose an initial notch length corresponding to 10% of the specimen width and a distance between inclusion centers of 24 [mm]. Symmetry is employed and one-quarter of the geometry is modeled with relevant symmetric boundary conditions as illustrated in Fig. A.16 (note that we may employ symmetric boundary conditions in this instance since the center inclusion is not shifted).

Identical elastic material parameters are used for all three models, corresponding to those provided in Section 3.3. Each model is subjected to a representative prescribed displacement of 7.5 [mm] which corresponds to 15 [mm] of stretch when symmetry is not employed. The plane stress assumption is then justified using the plots of the strain energy density in Fig. A.18, along the lines shown in Fig. A.17 (note that these two regions correspond to those in which cracks typically initiate). Additionally we provide the relevant force-displacement curves for the global problem in Fig. A.19.

The strain energy density near the notch tip is clearly best approximated in two-dimensions via a plane stress assumption as evidenced by the line plot in Fig. A.18(a). The strain energy density between inclusions illustrated in Fig. A.18(b) follows the same general trend as shown for the three-dimensional case, however, plane stress slightly under-predicts this quantity due to the out-of-plane stiffening effect of the rigid inclusions. This stiffening effect also manifests itself in terms of the

overall force versus displacement curves provided in Section 4.2. For a distance between inclusions of 18 [*mm*] the under-predicted stiffness is clearly visible. However, for the geometry investigated in this section, Fig. A.19 shows very minor stiffness deviation with respect to the three-dimensional formulation. It is also clear from this figure that a plane strain approximation significantly over-predicts the external load, further justifying the use of the plane stress approximation used in this work.

Appendix B. Force-displacement correlation with failure sequences

Here we briefly illustrate a few key points on the force-displacement curves previously presented, correlated with the system state for two representative examples: one in which the initial crack forms between inclusions and one in which it initiates from the notch tip. These two types of behavior are exhibited in the set of force-displacement curves provided in Section 4.2. Generally, initiation between inclusions is accompanied by a force-displacement response with a single peak and subsequent steep decline to zero force. This is demonstrated for N10D18 in Fig. B.20 with states A1-A2. In the other case, the crack initiates at the notch tip, propagates until it is arrested by the center inclusion, and stiffening occurs until either the crack continues around the inclusion or a secondary crack initiates between inclusions. This is demonstrated for the N10D30 case below with sequence snapshots labeled B1-B4.

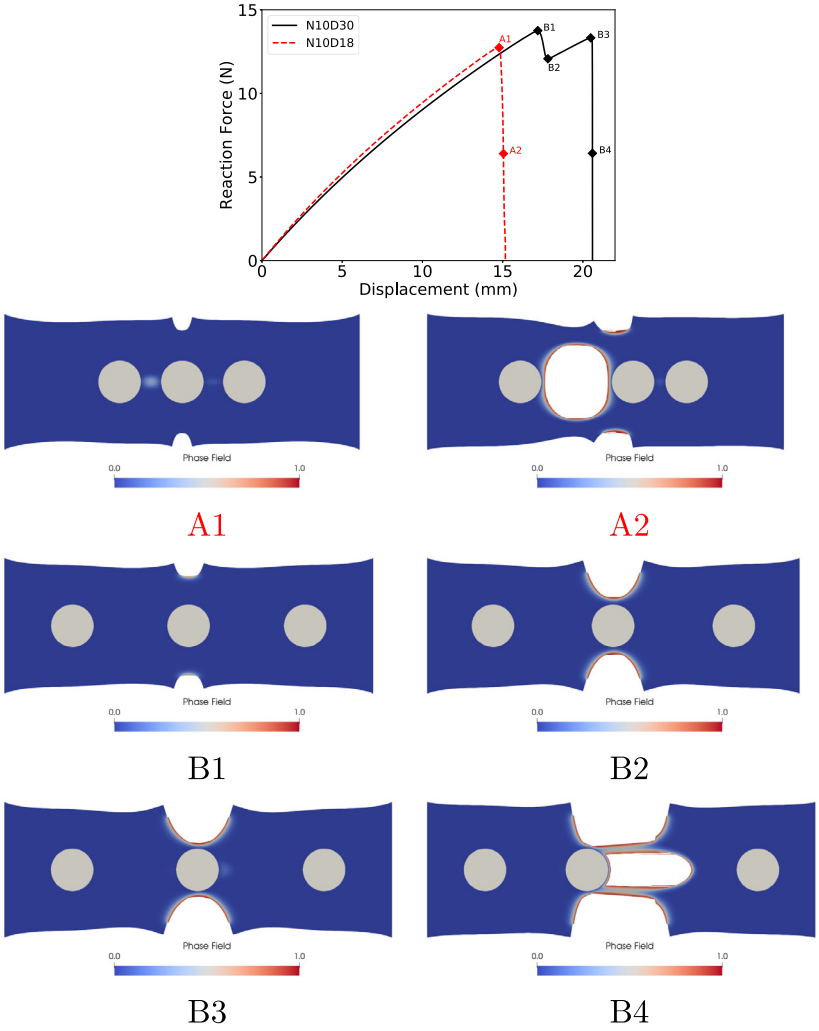


Fig. B.20. (A1 - A2) N10D18 and (B1 - B4) N10D30 numerical snapshots.

Appendix C. J-Integral calculations

In an effort to further analyze the crack initiation behavior of the phase field method employed herein, contour integrals are computed for certain geometries at the numerically predicted crack initiation point. The commercial finite element code, ABAQUS (aba, 2019), is used to perform the J-Integral (Rice, 1968) computation where the implementation follows the formulation of Shih et al. (1986).

Three different notch lengths (N05, N10, N20) are considered, with and without inclusions. These particular geometries were selected since cracks clearly initiate at the notch tip rather than between rigid inclusions or in the bulk material. This allows computation and comparison of the J-Integral values computed at the predicted initiation point (i.e. the notch tip). Generally, crack initiation in the phase field formulation is not clearly defined. Here we define initiation to occur when the peak value of the phase field at the notch-tip has reached 0.25, corresponding to the critical value analytically obtained by Borden et al. (2012) in the context of the standard phase field formulation (although it was derived for the small deformation case).

The same material properties presented previously are used in ABAQUS and a force-versus-displacement curve comparison is shown in Fig. C.21. A representative result is also provided in Fig. C.22 where the notch tip mesh is illustrated. It is expected that the value of the J-Integral is independent of the geometry at the crack initiation point when the material parameters are the same. Seven values are obtained for each geometry corresponding to seven different contour paths around the crack tip. The path-independence of the J-integral is clearly demonstrated in Table C.2. Although there is some variation in the converged value with respect to geometry, the variation is not very large. In light of this we conclude that the phase field formulation employed herein predicts crack growth to occur when approximately the same strain energy release rate is achieved. Nevertheless, more investigations of this type for different geometries are likely needed in order to draw a stronger conclusion.

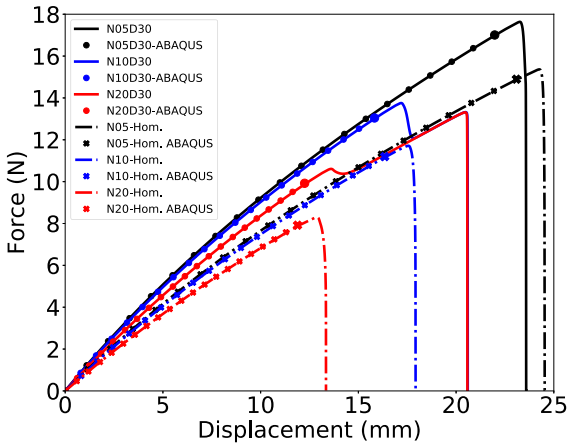


Fig. C.21. Force vs. displacement comparison with ABAQUS. The final ABAQUS marker (which is enlarged) represents the load at which we define crack initiation in each case. Note that "Hom." refers to predictions with homogeneous TP material (i.e. geometry without stiff inclusions).

Table C.2
J-Integral values computed for 6 geometries.

	Contour Path						
	1	2	3	4	5	6	7
N05	0.478	0.478	0.478	0.477	0.477	0.477	0.477
N10	0.503	0.502	0.502	0.501	0.501	0.501	0.501
N20	0.518	0.517	0.517	0.517	0.516	0.516	0.516
N05D30	0.481	0.481	0.481	0.480	0.480	0.480	0.480
N10D30	0.507	0.506	0.506	0.506	0.506	0.505	0.505
N20D30	0.524	0.523	0.523	0.523	0.523	0.522	0.522
Mean	0.502	0.501	0.501	0.501	0.501	0.500	0.500
Std. Dev.	0.019	0.019	0.019	0.019	0.019	0.019	0.019

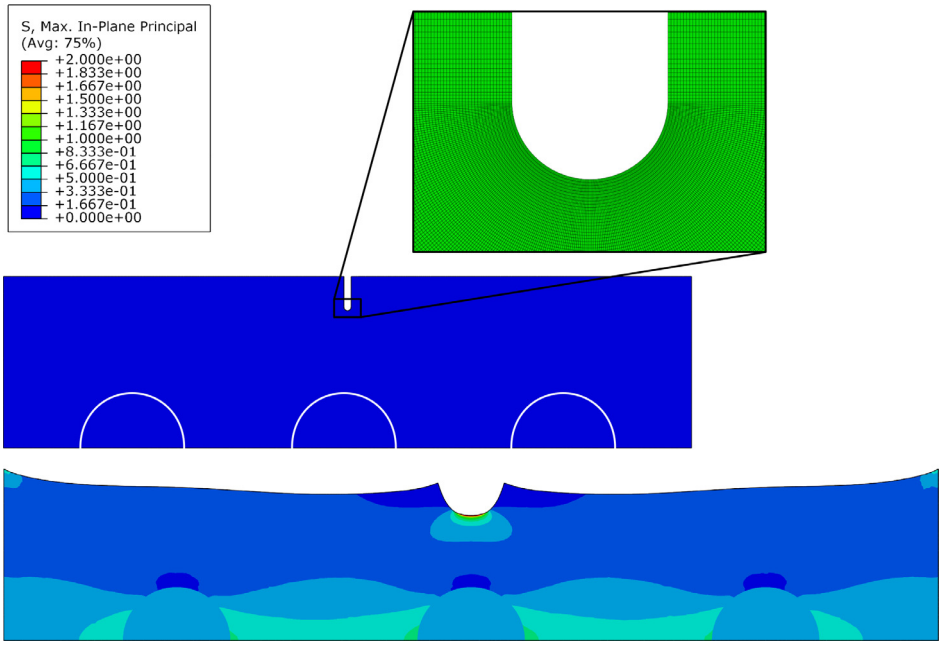


Fig. C.22. ABAQUS result illustration for the N10D30 geometry and notch-tip mesh used for the J-Integral calculation. Note that symmetry along the horizontal plane is employed. Both the undeformed and deformed configurations are presented where the contours illustrate the maximum in-plane principal stress distribution.

References

ABAQUS/Standard User's Manual, Version 2019, Dassault Systèmes Simulia Corp, United States, 2019.

Ambati, M., Gerasimov, T., De Lorenzis, L., 2015. A review on phase-field models of brittle fracture and a new fast hybrid formulation. Comput. Mech. 55 (2), 383–405. doi:10.1007/s00466-014-1109-y.

Ambati, M., Kruse, R., De Lorenzis, L., 2016. A phase-field model for ductile fracture at finite strains and its experimental verification. Comput. Mech. 57 (1), 149–167. doi:10.1007/s00466-015-1225-3.

Amor, H., Marigo, J.-J., Maurini, C., 2009. Regularized formulation of the variational brittle fracture with unilateral contact: numerical experiments. J. Mech. Phys. Solids 57 (8), 1209–1229. doi:10.1016/j.jmps.2009.04.011.

Arndt, D., Bangerth, W., Clevenger, T.C., Davydov, D., Fehling, M., Garcia-Sanchez, D., Harper, G., Heister, T., Heltai, L., Kronbichler, M., Kynch, R.M., Maier, M., Pelteret, J.-P., Turcksin, B., Wells, D., 2019. The `library, version 9.1`. J. Numer. Math. doi:10.1515/jnma-2019-0064. Accepted.

Arora, N., Batan, A., Li, J., Slesarenko, V., Rudykh, S., 2019. On the Influence of Inhomogeneous Interphase Layers on Instabilities in Hyperelastic Composites. Materials 12 (5), 763. doi:10.3390/ma12050763. https://www.mdpi.com/1996-1944/12/5/763.

Arriaga, M., Waisman, H., 2017. Combined stability analysis of phase-field dynamic fracture and shear band localization. Int. J. Plast. 96, 81–119.

Balay, S., Abhyankar, S., Adams, M.F., Brown, J., Brune, P., Buschelman, K., Dalcin, L., Dener, A., Eijkhout, V., Gropp, W.D., Karpeyev, D., Kaushik, D., Knepley, M.G., May, D.A., McInnes, L.C., Mills, R.T., Munson, T., Rupp, K., Sanan, P., Smith, B.F., Zampini, S., Zhang, H., Zhang, H., 2019. PETSc Users Manual. Technical Report. Argonne National Laboratory. https://www.mcs.anl.gov/petsc.

Bilgen, C., Weinberg, K., 2019. On the crack-driving force of phase-field models in linearized and finite elasticity. Computer Methods in Applied Mechanics and Engineering 353, 348–372. doi:10.1016/j.cma.2019.05.009. http://www.sciencedirect.com/science/article/pii/S0045782519302786.

Bonet, J., Wood, R.D., 2008. Nonlinear Continuum Mechanics for Finite Element Analysis, 2 Cambridge University Press doi:10.1017/CBO9780511755446.

Borden, M.J., 2012. Isogeometric analysis of phase-field models for dynamic brittle and ductile fracture thesis.

Borden, M.J., Hughes, T.J.R., Landis, C.M., Anvari, A., Lee, I.J., 2016. A phase-field formulation for fracture in ductile materials: Finite deformation balance law derivation, plastic degradation, and stress triaxiality effects. Computer Methods in Applied Mechanics and Engineering 312, 130–166. doi:10.1016/j.cma.2016.09.005. http://www.sciencedirect.com/science/article/pii/S0045782516311069.

Borden, M.J., Verhoosel, C.V., Scott, M.A., Hughes, T.J.R., Landis, C.M., 2012. A phase-field description of dynamic brittle fracture. Comput. Method. Appl. Mech. Eng. 217–220, 77–95. doi:10.1016/j.cma.2012.01.008.

Bourdin, B., Francfort, G.A., Marigo, J.-J., 2008. The variational approach to fracture. J. Elast. 91 (1–3), 5–148. doi:10.1007/s10659-007-9107-3.

Choo, J., Sun, W., 2018. Coupled phase-field and plasticity modeling of geological materials: From brittle fracture to ductile flow. Computer Methods in Applied Mechanics and Engineering 330, 1–32. doi:10.1016/j.cma.2017.10.009. http://www.sciencedirect.com/science/article/pii/S0045782517306783.

Dimas, L.S., Bratzel, G.H., Eylon, I., Buehler, M.J., 2013. Tough composites inspired by mineralized natural materials: Computation, 3d printing, and testing. Advanced Functional Materials 23 (36), 4629–4638. doi:10.1002/adfm.201300215. ISBN: 1616-3028.

Duda, F.P., Ciarbonetti, A., Sánchez, P.J., Huespe, A.E., 2015. A phase-field/gradient damage model for brittle fracture in elastic-plastic solids. Int. J. Plast. 65, 269–296.

Faye, A., Lev, Y., Volokh, K.Y., 2019. The effect of local inertia around the crack-tip in dynamic fracture of soft materials. Mech. Soft Mater. 1, 4. doi:10.1007/s42558-019-0004-2. http://adsabs.harvard.edu/abs/2019MecSM...1....4F.

Francfort, G.A., Marigo, J.J., 1998. Revisiting brittle fracture as an energy minimization problem. J. Mech. Phys. Solids 46 (8), 1319–1342. doi:10.1016/S0022-5096(98)00034-9.

Greenhalgh, E.S., 2009. Failure analysis and fractography of polymer composites. CRC press.

Gu, G.X., Takaffoli, M., Buehler, M.J., 2017. Hierarchically Enhanced Impact Resistance of Bioinspired Composites. Advanced Materials 29 (28), 1700060. 00072.

Gltekin, O., Dal, H., Holzapfel, G.A., 2018. Numerical aspects of anisotropic failure in soft biological tissues favor energy-based criteria: A rate-dependent anisotropic crack phase-field model. Computer Methods in Applied Mechanics and Engineering 331, 23–52. doi:10.1016/j.cma.2017.11.008. http://www.sciencedirect.com/science/article/pii/S0045782517307132.

Hauseux, P., Hale, J.S., Cotin, S., Bordas, S.P.A., 2018. Quantifying the uncertainty in a hyperelastic soft tissue model with stochastic parameters. Applied Mathematical Modelling 62, 86–102. doi:10.1016/j.apm.2018.04.021. http://www.sciencedirect.com/science/article/pii/S0307904X18302063.

Heister, T., Wheeler, M.F., Wick, T., 2015. A primal-dual active set method and predictor-corrector mesh adaptivity for computing fracture propagation using a phase-field approach. Computer Methods in Applied Mechanics and Engineering 290, 466–495. doi:10.1016/j.cma.2015.03.009. http://www.sciencedirect.com/science/article/pii/S0045782515001115.

Hesch, C., Gil, A.J., Ortigosa, R., Dittmann, M., Bilgen, C., Betsch, P., Franke, M., Janz, A., Weinberg, K., 2017. A framework for polyconvex large strain phase-field methods to fracture. Computer Methods in Applied Mechanics and Engineering 317, 649–683. doi:10.1016/j.cma.2016.12.035. http://www.sciencedirect.com/science/article/pii/S0045782516309677.

Hesch, C., Weinberg, K., 2014. Thermodynamically consistent algorithms for a finite-deformation phase-field approach to fracture. International Journal for Numerical Methods in Engineering 99 (12), 906–924. doi:10.1002/nme.4709. https://onlinelibrary.wiley.com/doi/abs/10.1002/nme.4709.

Hocine, N.A., Abdelaziz, M.N., Imad, A., 2002. Fracture problems of rubbers: j-integral estimation based upon factors and an investigation on the strain energy density distribution as a local criterion. Int. J. Fract. 117 (1), 1–23. doi:10.1023/A:1020967429222.

Jia, Z., Yu, Y., Hou, S., Wang, L., 2019. Biomimetic architected materials with improved dynamic performance. Journal of the Mechanics and Physics of Solids 125, 178–197. 00008.

Kumar, A., A. Francfort, G., Lopez-Pamies, O., 2018. Fracture and healing of elastomers: Aphase-transition theory and numerical implementation. Journal of the Mechanics and Physics of Solids 112, 523–551. doi:10.1016/j.jmps.2018.01.003. http://www.sciencedirect.com/science/article/pii/S0022509617309481.

Li, J., Rudykh, S., 2019. Tunable microstructure transformations and auxetic behavior in 3D-printed multiphase composites: The role of inclusion distribution. Compos. Part B 172, 352–362. doi:10.1016/j.compositesb.2019.05.012. http://www.sciencedirect.com/science/article/pii/S1359836818342574.

Li, J., Slesarenko, V., Galich, P.I., Rudykh, S., 2018. Instabilities and pattern formations in 3D-printed deformable fiber composites. Compos. Part B 148, 114–122. doi:10.1016/j.compositesb.2018.04.049. http://www.sciencedirect.com/science/article/pii/S1359836818303159.

Li, J., Slesarenko, V., Rudykh, S., 2018. Auxetic multiphase soft composite material design through instabilities with application for acoustic metamaterials. Soft Matter 14 (30), 6171–6180. doi:10.1039/C8SM00874D. https://pubs.rsc.org/en/content/articlelanding/2018/sm/c8sm00874d.

Li, Y., Kaynia, N., Rudykh, S., Boyce, M.C., 2013. Wrinkling of Interfacial Layers in Stratified Composites. Advanced Engineering Materials 15 (10), 921–926. doi:10.1002/adem.201200387. https://onlinelibrary.wiley.com/doi/abs/10.1002/adem.201200387.

Libonati, F., Gu, G.X., Qin, Z., Vergani, L., Buehler, M.J., 2016. Bone-Inspired Materials by Design: Toughness Amplification Observed Using 3d Printing and Testing. Advanced Engineering Materials 18 (8), 1354–1363. doi:10.1002/adem.201600143. ISBN: 0001410105.

Liu, L., Li, Y., 2018. Predicting the mixed-mode I/II spatial damage propagation along 3d-printed soft interfacial layer via a hyperelastic softening model. Journal of the Mechanics and Physics of Solids 116, 17–32. 00010.

Loew, P.J., Peters, B., Beex, L.A.A., 2019. Rate-dependent phase-field damage modeling of rubber and its experimental parameter identification. Journal of the Mechanics and Physics of Solids 127, 266–294. doi:10.1016/j.jmps.2019.03.022. http://www.sciencedirect.com/science/article/pii/S0022509618310433.

Mao, Y., Anand, L., 2018. A theory for fracture of polymeric gels. Journal of the Mechanics and Physics of Solids 115, 30–53. doi:10.1016/j.jmps.2018.02.008. http://www.sciencedirect.com/science/article/pii/S0022509617309730.

McAuliffe, C., Waisman, H., 2015. A unified model for metal failure capturing shear banding and fracture. International Journal of Plasticity 65, 131–151. doi:10.1016/j.ijplas.2014.08.016. http://www.sciencedirect.com/science/article/pii/S0749641914001831.

Miehe, C., Hofacker, M., Welschinger, F., 2010. A phase field model for rate-independent crack propagation: robust algorithmic implementation based on operator splits. Comput. Methods Appl. Mech. Eng. 199 (45), 2765–2778. doi:10.1016/j.cma.2010.04.011.

Miehe, C., Mauthe, S., 2016. Phase field modeling of fracture in multi-physics problems. part iii. crack driving forces in hydro-poro-elasticity and hydraulic fracturing of fluid-saturated porous media. Comput. Methods Appl. Mech. Eng. 304, 619–655.

Miehe, C., Schnzel, L.-M., 2014. Phase field modeling of fracture in rubbery polymers. part i: Finite elasticity coupled with brittle failure. Journal of the Mechanics and Physics of Solids 65, 93–113. doi:10.1016/j.jmps.2013.06.007. http://www.sciencedirect.com/science/article/pii/S0022509613001191.

Miehe, C., Schnzel, L.-M., Ulmer, H., 2015. Phase field modeling of fracture in multi-physics problems. Part I. Balance of crack surface and failure criteria for brittle crack propagation in thermo-elastic solids. Computer Methods in Applied Mechanics and Engineering 294, 449–485. doi:10.1016/j.cma.2014.11.016. http://www.sciencedirect.com/science/article/pii/S0045782514004423.

Miehe, C., Welschinger, F., Hofacker, M., 2010. Thermodynamically consistent phase-field models of fracture: variational principles and multi-field FE implementations. Int. J. Numer. Methods Eng. 83 (10), 1273–1311. doi:10.1002/nme.2861.

Mikelić, A., Wheeler, M.F., Wick, T., 2015. Phase-field modeling of a fluid-driven fracture in a poroelastic medium. Comput. Geosci. 19 (6), 1171–1195. doi:10.1007/s10596-015-9532-5.

Nguyen, T.T., Yvonnet, J., Bornert, M., Chateau, C., 2016. Initiation and propagation of complex 3d networks of cracks in heterogeneous quasi-brittle materials: direct comparison between in situ testing-microct experiments and phase field simulations. J. Mech. Phys. Solids 95, 320–350.

Paggi, M., Reinoso, J., 2017. Revisiting the problem of a crack impinging on an interface:a modeling framework for the interaction between the phase field approach for brittle fracture and the interface cohesive zone model. Comput. Methods Appl. Mech. Eng. 321, 145–172.

Polyjet, 2018. 3d printers systems and materials overview. https://www.stratasys.com/-/media/files/printer-spec-sheets/polyjet-3d-printers-systems-materials-spec-sheet.pdf.

Raayai-Ardakani, S., RachelleEarl, D., Cohen, T., 2019. The intimate relationship between cavitation and fracture. Soft Matter 15 (25), 4999–5005. doi:10.1039/C9SM00570F. https://pubs.rsc.org/en/content/articlelanding/2019/sm/c9sm00570f.

Raina, A., Miehe, C., 2016. A phase-field model for fracture in biological tissues. Biomech. Model. Mechanobiol. 15 (3), 479–496. doi:10.1007/s10237-015-0702-0.

Rappel, H., Beex, L.A.A., Hale, J.S., Noels, L., Bordas, S.P.A., 2019. A tutorial on bayesian inference to identify material parameters in solid mechanics. Arch. Comput. Methods Eng. doi:10.1007/s11831-018-09311-x.

Rice, J.R., 1968. A Path Independent Integral and the Approximate Analysis of Strain Concentration by Notches and Cracks. Journal of Applied Mechanics 35 (2), 379–386. doi:10.1115/1.3601206. https://asmedigitalcollection.asme.org/appliedmechanics/article/35/2/379/392117/A-Path-Independent-Integral-and-the-Approximate.

Ritchie, R.O., 2011. The conflicts between strength and toughness. Nat. Mater. 10 (11), 817–822. doi:10.1038/nmat3115.

Rudykh, S., Boyce, M.C., 2014. Transforming Small Localized Loading into Large Rotational Motion in Soft Anisotropically Structured Materials. Advanced Engineering Materials 16 (11), 1311–1317. doi:10.1002/adem.201400162. https://onlinelibrary.wiley.com/doi/abs/10.1002/adem.201400162.

Rudykh, S., Ortiz, C., C. Boyce, M., 2015. Flexibility and protection by design: imbricated hybrid microstructures of bio-inspired armor. Soft Matter 11 (13), 2547–2554. doi:10.1039/C4SM02907K. https://pubs.rsc.org/en/content/articlelanding/2015/sm/c4sm02907k.

Ryvkin, M., Slesarenko, V., Cherkaev, A., Rudykh, S., 2020. Fault-tolerant elasticplastic lattice material. Philos. Trans. R. Soc. A. 00000.

Vero, 2018. material data sheet. https://www.stratasys.com/-/media/files/material-spec-sheets/vero-material-data-sheet.pdf.

San, B., Waisman, H., 2017. Optimization of Carbon Black Polymer Composite Microstructure for Rupture Resistance. Journal of Applied Mechanics 84 (2). doi:10.1115/1.4035050. https://asmedigitalcollection.asme.org/appliedmechanics/article/84/2/021005/422029/Optimization-of-Carbon-Black-Polymer-Composite.

Shen, R., Waisman, H., Yosibash, Z., Dahan, G., 2019. A novel phase field method for modeling the fracture of long bones. International Journal for Numerical Methods in Biomedical Engineering 35 (8), e3211. doi:10.1002/cnm.3211. E3211 cnm.3211. https://onlinelibrary.wiley.com/doi/pdf/10.1002/cnm.3211.

Shih, C.F., Moran, B., Nakamura, T., 1986. Energy release rate along a three-dimensional crack front in a thermally stressed body. Int. J. Fract. 30 (2), 79–102. doi:10.1007/BF00034019.

Slesarenko, V., Kazarinov, N., Rudykh, S., 2017. Distinct failure modes in bio-inspired 3d-printed staggered composites under non-aligned loadings. Smart Materials and Structures 26 (3), 035053. doi:10.1088/1361-665X/aa59eb. http://stacks.iop.org/0964-1726/26/i=3/a=035053?key=crossref.f1e195c2e179a6a0b3cc0fe556ebd49a.

Slesarenko, V., Rudykh, S., 2016. Harnessing viscoelasticity and instabilities for tuning wavy patterns in soft layered composites. Soft Matter 12 (16), 3677–3682. doi:10.1039/C5SM02949J. https://pubs.rsc.org/en/content/articlelanding/2016/sm/c5sm02949j.

Slesarenko, V., Rudykh, S., 2018. Towards mechanical characterization of soft digital materials for multimaterial 3d-printing. International Journal of Engineering Science 123, 62–72. doi:10.1016/j.ijengsci.2017.11.011. ArXiv: 1710.05187Publisher: Elsevier Ltd.

Slesarenko, V., Volokh, K.Y., Aboudi, J., Rudykh, S., 2017. Understanding the strength of bioinspired soft composites. International Journal of Mechanical Sciences 131-132, 171–178. doi:10.1016/j.ijmecsci.2017.06.054. http://linkinghub.elsevier.com/retrieve/pii/S0020740317306100.

Studart, A.R., 2016. Additive manufacturing of biologically-inspired materials. Chemical Society Reviews 45 (2), 359–376. 00160.

Talamini, B., Mao, Y., Anand, L., 2018. Progressive damage and rupture in polymers. Journal of the Mechanics and Physics of Solids 111, 434–457. doi:10.1016/j.jmps.2017.11.013. http://www.sciencedirect.com/science/article/pii/S0022509617303939.

Tang, S., Zhang, G., Guo, T.F., Guo, X., Liu, W.K., 2019. Phase field modeling of fracture in nonlinearly elastic solids via energy decomposition. Computer Methods in Applied Mechanics and Engineering 347, 477–494. doi:10.1016/j.cma.2018.12.035. http://www.sciencedirect.com/science/article/pii/S004578251830642X.

Teichtmeister, S., Kienle, D., Aldakheel, F., Keip, M.-A., 2017. Phase field modeling of fracture in anisotropic brittle solids. Int. J. Non Linear Mech. 97, 1–21.

Verhoosel, C.V., Borst, R.d., 2013. A phase-field model for cohesive fracture. International Journal for Numerical Methods in Engineering 96 (1), 43–62. doi:10.1002/nme.4553. https://onlinelibrary.wiley.com/doi/abs/10.1002/nme.4553.

Volokh, K.Y., 2010. On modeling failure of rubber-like materials. Mechanics Research Communications 37 (8), 684–689. doi:10.1016/j.mechrescom.2010.10.006. http://www.sciencedirect.com/science/article/pii/S0093641310001461.

Volokh, K.Y., 2011. Characteristic length of damage localization in rubber. Int. J. Fract. 168 (1), 113–116. doi:10.1007/s10704-010-9563-9.

Volokh, K.Y., 2017. Fracture as a material sink. Mater. Theory 1 (1), 3. doi:10.1186/s41313-017-0002-4.

Volokh, K.Y., Aboudi, J., 2016. Aneurysm strength can decrease under calcification. Journal of the Mechanical Behavior of Biomedical Materials 57, 164–174. doi:10.1016/j.jmbbm.2015.11.012. http://www.sciencedirect.com/science/article/pii/S1751616115004300.

Wang, X., Jian, M., Zhou, Z., Gou, J., Hui, D., 2017. 3D printing of polymer matrix composites: a review and prospective | elsevier enhanced reader. Compos. Part B (110) 442–458.

Wilson, Z.A., Landis, C.M., 2016. Phase-field modeling of hydraulic fracture. J. Mech. Phys. Solids. 96, 264–290.

Wu, J., McAuliffe, C., Waisman, H., Deodatis, G., 2016. Stochastic analysis of polymer composites rupture at large deformations modeled by a phase field method. Comput. Methods Appl. Mech. Eng. 312, 596–634. doi:10.1016/j.cma.2016.06.010.

Wu, J.-Y., Nguyen, V.P., Thanh Nguyen, C., Sutula, D., Bordas, S., Sinaie, S., 2019. Phase field modelling of fracture. Adv. Appl. Mech. 53. https://www.sciencedirect.com/science/article/pii/S0065215619300134.

Yin, B., Kaliske, M., 2019. Fracture simulation of viscoelastic polymers by the phase-field method. Comput. Mech. doi:10.1007/s00466-019-01769-1.

Yin, S., Yang, W., Kwon, J., Wat, A., Meyers, M.A., Ritchie, R.O., 2019. Hyperelastic phase-field fracture mechanics modeling of the toughening induced by Bouligand structures in natural materials. Journal of the Mechanics and Physics of Solids 131, 204–220. doi:10.1016/j.jmps.2019.07.001. http://www.sciencedirect.com/science/article/pii/S0022509619300584.